

Diagnoses to unravel secular hydrodynamical processes in rotating main sequence stars

T. Decressin^{1,2}, S. Mathis^{3,8}, A. Palacios⁴, L. Siess⁵, S. Talon⁶, C. Charbonnel^{1,7}, and J.-P. Zahn⁸

¹ Geneva Observatory, University of Geneva, chemin des Maillettes 51, 1290 Sauverny, Switzerland

² Argelander Institute for Astronomy (AIfA), Auf dem Hügel 71, 53121 Bonn, Germany
e-mail: decressin@astro.uni-bonn.de

³ Laboratoire AIM, CEA/DSM-CNRS-Université Paris Diderot, IRFU/SaP Centre de Saclay, 91191 Gif-sur-Yvette, France
e-mail: stephane.mathis@cea.fr

⁴ GRAAL, Université Montpellier II, CNRS, Place E. Bataillon, 34095 Montpellier Cedex 05, France

⁵ IAA-ULB, Université Libre de Bruxelles, Boulevard du Triomphe, CP 26, 1050 Bruxelles, Belgium

⁶ Réseau Québécois de Calcul de Haute Performance, Université de Montréal (DGTIC), CP 6128, succ. Centre-ville, Montréal H3C 3J7, Canada

⁷ LATT, CNRS UMR 5572, Université de Toulouse, 14 Av. Edouard Belin, 31400 Toulouse Cedex 04, France

⁸ LUTH, Observatoire de Paris-CNRS-Université Paris-Diderot, Place Jules Janssen, 92195 Meudon, France

Received 24 July 2008 / Accepted 18 November 2008

ABSTRACT

Context. Recent progress and constraints brought by helio and asteroseismology call for a better description of stellar interiors and an accurate description of rotation-driven mechanisms in stars.

Aims. We present a detailed analysis of the main physical processes responsible for the transport of angular momentum and chemical species in the radiative regions of rotating stars. We focus on cases where meridional circulation and shear-induced turbulence all that are included in the simulations (i.e., no either internal gravity waves nor magnetic fields). We put special emphasis on analysing the angular momentum transport loop and on identifying the contribution of each of the physical process involved.

Methods. We develop a variety of diagnostic tools designed to help disentangle the role of the various transport mechanisms. Our analysis is based on a 2-D representation of the secular hydrodynamics, which is treated using expansions in spherical harmonics. By taking appropriate horizontal averages, the problem reduces to one dimension, making it implementable in a 1D stellar evolution code, while preserving the advective character of angular momentum transport. We present a full reconstruction of the meridional circulation and of the associated fluctuations of temperature and mean molecular weight, along with diagnosis for the transport of angular momentum, heat, and chemicals. In the present paper these tools are used to validate the analysis of two main sequence stellar models of 1.5 and 20 M_{\odot} , for which the hydrodynamics has previously been extensively studied in the literature.

Results. We obtain a clear visualisation and a precise estimation of the different terms entering the angular momentum and heat transport equations in radiative zones of rotating stars. This enables us to corroborate the main results obtained over the past decade by Zahn, Maeder, and collaborators concerning the secular hydrodynamics of such objects. We focus on the meridional circulation driven by angular momentum losses and structural readjustments. We confirm quantitatively for the first time through detailed computations and separation of the various components that the advection of entropy by this circulation is balanced very well by the barotropic effects and the thermal relaxation during most of the main sequence evolution. This enables us to simplify for the thermal relaxation on this phase. The meridional currents in turn advect heat and generate temperature fluctuations that induce differential rotation through thermal wind, thus closing the transport loop. We plan to make use of our refined diagnosis tools in forthcoming studies of secular (magneto-)hydrodynamics of stars at various evolutionary stages.

Key words. hydrodynamics – turbulence – stars: evolution – stars: rotation

1. The impact of rotation on stellar evolution

Rotation, and more precisely differential rotation, has a major impact on the internal dynamics of stars, in several ways. It induces large-scale circulations both in radiative and convective zones that simultaneously advect angular momentum, nuclides, and magnetic fields (Eddington 1925; Vogt 1925; Sweet 1950; Mestel 1953; Busse 1982; Zahn 1992; Talon 1997; Talon et al. 1997; Maeder & Zahn 1998; Meynet & Maeder 2000; Garaud 2002b; Palacios et al. 2003, 2006; Mathis & Zahn 2004, 2005; Rieutord 2006a; Espinosa Lara & Rieutord 2007; Mathis et al. 2007). When the star rotates differentially, various instabilities develop (secular and dynamical shear instabilities, baroclinic,

and multidiffusive instabilities) that generate hydrodynamical turbulence in radiative zones, in addition to these circulations. Just as in the terrestrial atmosphere and in laboratory experiments, this turbulence acts to reduce its cause, namely the gradients of angular velocity and of chemical composition. This explains why its effect may be described as a diffusion process (Talon & Zahn 1997; Maeder 2003; Mathis et al. 2004; Talon 2007, and references therein).

Rotating stars have an equator that is cooler than the poles, which has a strong effect on radiatively driven stellar winds and hence on the loss of mass and angular momentum (Maeder 1999). If rotation is large enough, the stars can even reach the break-up limit, when centrifugal force balances the gravity, and

matter is ejected through an equatorial mechanical winds that create a circumstellar disk (Maeder & Meynet 2000a; Meynet et al. 2007; Ekström et al. 2008).

Rotation also has a strong impact on the stellar magnetism. In radiative zones, rotation interacts with the magnetic field and is able to trigger magnetohydrodynamical instabilities, which could play a role in the transport of angular momentum and nuclides (Charbonneau & MacGregor 1993; Garaud 2002a; Spruit 1999, 2002; Menou et al. 2004; Maeder & Meynet 2004; Eggenberger et al. 2005; Braithwaite & Spruit 2005; Mathis & Zahn 2005; Braithwaite 2006; Brun & Zahn 2006; Zahn et al. 2007). Furthermore, internal gravity waves and gravito-inertial waves that are excited at the edge of the convection zones may also contribute to the transport of angular momentum. They propagate inside radiative zones and extract or deposit angular momentum in the region where they are damped, thus modifying the angular velocity profile and the vertical distribution of chemicals (Press 1981; Schatzman 1993; Talon et al. 2002; Talon & Charbonnel 2003, 2004, 2005, 2008; Charbonnel & Talon 2005; Rogers & Glatzmaier 2005; Pantillon et al. 2007; Mathis et al. 2008).

All these effects significantly modify the evolution of rotating stars. They affect their surface velocities and chemical abundances, and change their paths across the colour-magnitude diagram (Maeder & Meynet 2000b; Maeder 2009). They also modify the internal structure of stars in a way that we will soon be able to test thanks to asteroseismology over a broader range of evolutionary phases.

In this paper we present a set of diagnosis tools adapted to the analysis of stellar evolution with rotation and use them to compare the efficiency of different transport processes. The present study focuses on “type I rotational transport”, where magnetic fields and waves are not accounted for and where the angular momentum and the nuclides are both transported exclusively by meridional circulation and shear-induced turbulence. These diagnoses and tools rely on a specific expansion of the equations for the transport of angular momentum, heat, and chemicals that are briefly recalled in Sect. 2. In Sect. 3, we validate our method by applying our tools to two specific stellar models for which the hydrodynamics has already been extensively studied in the literature. Conclusions and perspectives are presented in Sect. 4.

2. Modelling the secular processes

2.1. Scale separation

To simulate the dynamical processes in a star in full details, would require including length scales and time scales spanning many orders of magnitude. This is clearly not feasible, even with the most powerful computers. Either one chooses to describe what occurs on a dynamical time scale, such as a convective turnover time or one focuses on the long time evolution, as we do here, where the typical time is either the Kelvin-Helmholtz time or that characterising the dominant nuclear reactions. The same is true for the length scales, at least in the vertical direction, where we take the resolution that adequately represents the steepest gradients that develop during the evolution.

The situation is somewhat different in the horizontal direction – i.e. in latitude, since we consider only the axisymmetric case here –. Stellar radiative zones are stably stratified regions, and the buoyancy, which is the restoring force, acts to inhibit turbulent motions in the vertical direction. This leads to a strongly anisotropic turbulent transport that is more efficient in the horizontal direction (along isobars) than in the vertical one. As a

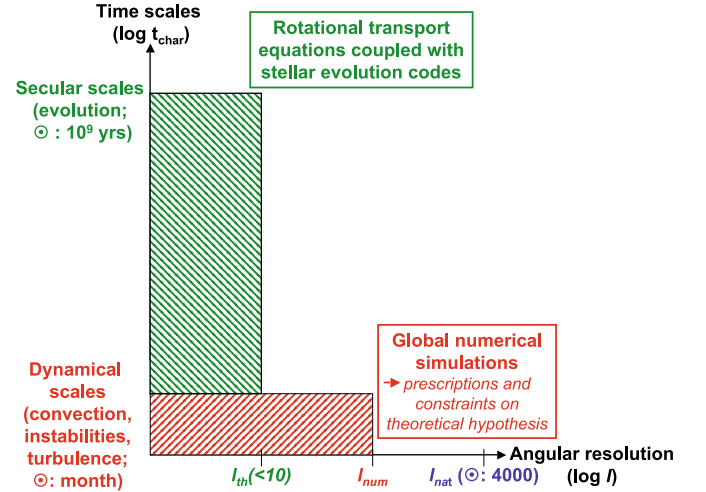


Fig. 1. Modelling strategy to study dynamical stellar evolution. The diagram presents time scales of the typical physical processes as a function of the angular resolution needed to properly describe these processes. The angular resolution is expressed in terms of the l index of the spherical harmonics $Y_{l,m}(\theta, \phi)$. $l_{\text{num}} \approx 600$ indicates the maximum angular resolution (in terms of spherical harmonics nodes) presently achieved in global numerical simulations.

result, the horizontal gradients of all scalar fields (temperature, angular velocity, etc.) are much smaller than their vertical gradients, which allows their expansion in a few spherical harmonics. This scale separation, both in space and in time, is illustrated in Fig. 1.

Considering the axisymmetric case, each scalar field is thus written as the sum of its horizontal average on an isobar, and its associated fluctuation, which is expanded in the Legendre polynomials basis $P_\ell(\cos \theta)$, up to some maximum order ℓ_{th} . For simplicity’s sake, we present here the results keeping a single scale $\ell = 2$, which is dominant. Let us note that there are circumstances where we have to include many more components, for instance when dealing with magnetic fields.

The unresolved scales intervene in the turbulent transport, for which a prescription is applied that is derived, whenever possible, from laboratory experiments or numerical simulations, and if not through phenomenological considerations.

2.2. Linearization and expansion in spherical harmonics

Let us briefly recall how these expansions are performed in practice; for more details, we refer the reader to Mathis & Zahn (2004) and Maeder (2009). We begin with the macroscopic velocity field, which is split into 3 components:

$$\mathbf{V} = \underbrace{r \sin \theta \Omega(r, \theta) \widehat{\mathbf{e}}_\varphi}_1 + \underbrace{\dot{r} \widehat{\mathbf{e}}_r}_2 + \underbrace{\mathbf{U}_M(r, \theta)}_3. \quad (1)$$

Term 1 represents the azimuthal velocity field associated with the differential rotation. Term 2 corresponds to the radial Lagrangian velocity due to the structural readjustments of the star during its evolution. Term 3 is the meridional circulation velocity field. $\widehat{\mathbf{e}}_k$ where $k = \{r, \theta, \varphi\}$ are the unit vectors in the radial, latitudinal, and azimuthal directions.

In radiative zones, because of the strong stratification, the turbulent transport is highly anisotropic, which leads to a “shellular” rotation profile (Zahn 1992). The angular velocity thus varies little on an isobar, allowing to expand it as

$$\Omega(r, \theta) = \overline{\Omega}(r) + \Omega_2(r) [P_2(\cos \theta) - 1/5], \quad (2)$$

where

$$\overline{\Omega}(r) = \frac{\int_0^\pi \sin^3 \theta \Omega(r, \theta) d\theta}{\int_0^\pi \sin^3 \theta d\theta}. \quad (3)$$

As usual, the meridional velocity field is projected on spherical functions, of which we show here only that of lowest order:

$$\mathbf{U}_M = U_2(r) P_2(\cos \theta) \widehat{\mathbf{e}}_r + V_2(r) \frac{dP_2(\cos \theta)}{d\theta} \widehat{\mathbf{e}}_\theta, \quad (4)$$

where P_2 is the second-order Legendre polynomial. The anelastic approximation is adopted, filtering out the acoustic waves, which is amply justified for this slow meridional circulation. Therefore, the continuity equation reduces to $\nabla \cdot (\overline{\rho} \mathbf{U}_M) = 0$, which leads to the following relation between the latitudinal (V_2) and the radial (U_2) amplitude functions:

$$V_2 = \frac{1}{6\overline{\rho}r} \partial_r (\overline{\rho} r^2 U_2). \quad (5)$$

Moreover, since $\overline{\rho} \mathbf{U}_M$ is divergenceless, it may be expressed using a stream function ($\xi_M(r, \theta)$) as in Spiegel & Zahn (1992), where

$$\overline{\rho} \mathbf{U}_M = -\frac{1}{r \sin \theta} \nabla \xi \times \widehat{\mathbf{e}}_\varphi, \quad (6)$$

which leads to

$$\overline{\rho} \mathbf{U}_{M,r} = -\frac{1}{r^2 \sin \theta} \partial_\theta \xi_M \quad \text{and} \quad \overline{\rho} \mathbf{U}_{M,\theta} = \frac{1}{r \sin \theta} \partial_r \xi_M \quad (7)$$

with

$$\xi_M = \frac{1}{2} \overline{\rho} r^2 U_2 (\cos^3 \theta - \cos \theta). \quad (8)$$

The quantity $\overline{\rho} \mathbf{U}_M$, and thus \mathbf{U}_M , are then tangent to the iso- ξ lines since $\mathbf{U}_M \cdot \nabla \xi = 0$ (cf. Eq. (6)).

Finally, all other variables are expanded as shown here for the temperature and the mean molecular weight:

$$T(r, \theta) = \overline{T}(r) + \delta T(r, \theta) \quad \text{with} \quad \delta T(r, \theta) = [\Psi_2(r) \overline{T}] P_2(\cos \theta) \quad (9)$$

and

$$\mu(r, \theta) = \overline{\mu}(r) + \delta \mu(r, \theta) \quad \text{with} \quad \delta \mu(r, \theta) = [\Lambda_2(r) \overline{\mu}] P_2(\cos \theta); \quad (10)$$

here, \overline{T} and $\overline{\mu}$ are the horizontal averages, δT and $\delta \mu$ being their fluctuations and Ψ_2 and Λ_2 their relative fluctuations on the isobar.

2.3. The transport equations

Using these notations, the transport equations for angular momentum and chemicals may thus be expanded in the following way.

2.3.1. Transport of angular momentum and thermal-wind

We first consider the azimuthal projection of the momentum equation. By averaging it over an isobar, we obtain the following advection-diffusion equation for the mean angular momentum:

$$\overline{\rho} \frac{d}{dt} (r^2 \overline{\Omega}) = \underbrace{\frac{1}{5r^2} \partial_r (\overline{\rho} r^4 \overline{\Omega} U_2)}_1 + \underbrace{\frac{1}{r^2} \partial_r (\overline{\rho} v_v r^4 \partial_r \overline{\Omega})}_2. \quad (11)$$

Term 1 represents the transport of angular momentum by the meridional circulation; note that the advective character of that transport is preserved. The diffusion term 2 is associated with the action of the shear-induced turbulence, where v_v is the turbulent viscosity in the vertical direction (see below Eq. (28)). The Lagrangian time derivative d/dt is defined as $d/dt = \partial_t + \dot{r} \partial_r$.

This equation shows the relation between the meridional circulation and the transport of angular momentum. In the asymptotic regime, the left hand side term is zero and the transport of angular momentum by meridional circulation is exactly balanced by that through shear turbulence. In the limit of vanishing turbulent viscosity, the rotation profile would adjust so that no meridional currents appear (Busse 1982). In reality, because of the loss of angular momentum by the wind and/or its redistribution by structural changes, the left hand side term is non zero.

By integrating Eq. (11) over a surface of radius r , it can be recast in an equation for the fluxes:

$$\Gamma(m) = -F_{\text{tot}} = -F_{\text{MC}}(r) - F_S(r), \quad (12)$$

where

$$F_{\text{MC}}(r) = -\frac{1}{5} \overline{\rho} r^4 \overline{\Omega} U_2 \quad (13)$$

is the flux transported by the meridional circulation, and

$$F_S(r) = -\overline{\rho} r^4 v_v \partial_r \overline{\Omega} \quad (14)$$

is what is carried by the vertical shear induced turbulence. The term $\Gamma(m)$ represents the loss or gain of angular momentum inside the isobar enclosing the mass $m(r)$; its derivation is given in Appendix A:

$$\Gamma(m) = \frac{1}{4\pi} \frac{d}{dt} \left[\int_0^{m(r)} r'^2 \overline{\Omega} dm' \right]. \quad (15)$$

From Eq. (12) it is also possible to extract the radial component of the meridional circulation velocity:

$$U_2 = U_\Gamma + U_V = \frac{5}{\overline{\rho} r^4 \overline{\Omega}} \left[\Gamma(m) - \overline{\rho} v_v r^4 \partial_r \overline{\Omega} \right]. \quad (16)$$

Finally, by taking the curl of the momentum equation and again filtering out the fast time scales, we obtain the so-called thermal wind equation:

$$\frac{1}{3} r \partial_r \overline{\Omega}^2 = \frac{\overline{g}}{r} (\varphi \Lambda_2 - \delta \Psi_2), \quad (17)$$

where \overline{g} is the horizontal average of the effective gravity¹. The coefficients $\delta = -(\partial \ln \rho / \partial \ln T)_{P,\mu}$ and $\varphi = (\partial \ln \rho / \partial \ln \mu)_{P,T}$ are introduced by the generalised equation of state (Kippenhahn & Weigert 1990; see Maeder & Zahn 1998 or Mathis & Zahn 2004 for more details). The right hand term is the baroclinic torque $\frac{1}{\rho} \nabla \rho \times \mathbf{g}$.

2.3.2. Thermal relaxation

Likewise, by expanding the energy conservation equation over spherical functions, we establish the following equation for the

¹ In a rotating star, the centrifugal force diminishes the local gravity, and the effective gravity \overline{g} is then given by horizontally averaging the hydrostatic equilibrium: $\mathbf{g} = \nabla \Phi + \frac{1}{2} \Omega^2 \nabla (r \sin \theta)^2$, where Φ is the gravitational potential.

temperature perturbation represented here by Ψ_2 (Eq. (101) in Mathis & Zahn 2004; see Zahn 1992):

$$\underbrace{\overline{\rho T} C_p \frac{d\Psi_2}{dt}}_{\overline{\rho T} \partial, \bar{s}} = \underbrace{-\overline{\rho T} C_p \frac{N_T^2}{g\delta} U_2}_{\overline{\rho T} U, \partial, \bar{s}} + \underbrace{\overline{\rho} \frac{L}{M} \mathcal{T}_{2,B} + \overline{\rho} \frac{L}{M} \mathcal{T}_{2,Th}}_{\nabla \cdot (\chi \nabla T) - \nabla \cdot F_H} + \underbrace{\overline{\rho} \frac{L}{M} \mathcal{T}_{2,N-G}}_{\rho \varepsilon} \quad (18)$$

where N_T , the buoyancy frequency linked with the entropy stratification, is given by $N_T^2 = (\overline{g\delta}/H_P) (\nabla_{ad} - \nabla)$ with the usual notations for the temperature gradients: $\nabla = \partial \ln \overline{T} / \partial \ln P$. This is again an advection/diffusion equation, where the advective term plays the role of a heat source or sink, since the meridional circulation is caused by the transport of angular momentum, with the other terms essentially describing the thermal relaxation due to radiative damping. The entropy flux carried by the horizontal turbulence is $\nabla \cdot F_H$.

For diagnostic purposes (and also for historical reasons; see the discussion in Zahn 1992, after Eq. (3.32)), we split the diffusion term into two pieces, whose expressions are given in Appendix B:

- $\mathcal{T}_{2,B}$ corresponds to the divergence of the radiative flux associated to the deformation of the isobar induced by the perturbing force, which here is the centrifugal acceleration. This term subsists in the case of solid body rotation; for this reason, we called it the *barotropic* term following Zahn (1992).
- $\mathcal{T}_{2,Th}$ contains the highest derivatives of the diffusion operator, and according to the thermal wind Eq. (17), it vanishes in an homogeneous star when the rotation is uniform. It is referred to as the *thermic* or *baroclinic* term (Zahn 1992).

The last term $\mathcal{T}_{2,N-G}$ is associated with the nuclear reactions and radial structural readjustments during its evolution and usually plays a negligible role.

Equation (18) can finally be written in the following form

$$\tilde{\mathcal{T}}_{N-S} = \tilde{\mathcal{T}}_{Adv} + \tilde{\mathcal{T}}_B + \tilde{\mathcal{T}}_{Th} + \tilde{\mathcal{T}}_{N-G}, \quad (19)$$

where

$$\tilde{\mathcal{T}}_{NS} = \overline{\rho T} C_p \frac{d\Psi_2}{dt}, \quad (20)$$

$$\tilde{\mathcal{T}}_{Adv} = -\overline{\rho T} C_p \frac{N_T^2}{g\delta} U_2, \quad (21)$$

$$\tilde{\mathcal{T}}_B = \overline{\rho} \frac{L}{M} \mathcal{T}_{2,B}, \quad (22)$$

$$\tilde{\mathcal{T}}_{Th} = \overline{\rho} \frac{L}{M} \mathcal{T}_{2,Th}, \quad (23)$$

$$\tilde{\mathcal{T}}_{N-G} = \overline{\rho} \frac{L}{M} \mathcal{T}_{2,N-G}. \quad (24)$$

This will be used in Sect. 3.4. in our diagnosis tools.

2.3.3. Transport of nuclides

The expansion of the transport equation for the nuclides on an isobar leads to an equation for the evolution of the mass fraction of each considered chemical (see also Meynet & Maeder 2000):

$$\left(\frac{dX_i}{dt} \right)_{M_r} = \frac{\partial}{\partial M_r} \left[(4\pi r^2 \rho)^2 (D_v + D_{eff}) \frac{\partial X_i}{\partial M_r} \right] + \left(\frac{dX_i}{dt} \right)_{nucl}, \quad (25)$$

where $dM_r = 4\pi \overline{\rho} r^2 dr$ and D_v is the vertical component of the turbulent diffusivity (see Eq. (28) below). The strong horizontal turbulence leads to the erosion of the advective transport, which can then be described as a diffusive process (Chaboyer & Zahn 1992) with the following effective diffusion coefficient

$$D_{eff} = \frac{(rU_2)^2}{30D_h}, \quad (26)$$

where D_h is the horizontal component of the turbulent diffusivity (see Eqs. (29) and (30)). The second term on the right hand side of Eq. (25) corresponds to the temporal mass fraction evolution of the i th nuclide due to nuclear burning.

Equation (25) is complemented by an equation for the time evolution of the relative fluctuation of the mean molecular weight, expressed here in terms of Λ_2 :

$$\frac{d\Lambda_2}{dt} - \frac{d \ln \overline{\mu}}{dt} \Lambda_2 = \frac{N_\mu^2}{g\varphi} U_2 - \frac{6}{r^2} D_h \Lambda_2, \quad (27)$$

where N_μ , the chemical part of the Brunt-Väisälä frequency, is given by $N_\mu^2 = (\overline{g\varphi}/H_P) \nabla_\mu$ with $\nabla_\mu = \partial \ln \overline{\mu} / \partial \ln P$.

2.3.4. Turbulence modelling

The details of turbulence modelling have already been extensively discussed in previous papers (Talon et al. 1997; Palacios et al. 2006), so that we just recall here the expressions we have chosen.

For the vertical turbulent diffusion coefficients ($D_v \simeq \nu_v$), we use the expression by Talon & Zahn (1997):

$$D_v = \frac{Ri_c}{N_T^2 / (K_T + D_h) + N_\mu^2 / D_h} (r\partial_r \overline{\Omega})^2, \quad (28)$$

where $Ri_c = 1/6$ is the adopted value for the critical Richardson number and K_T the thermal diffusivity.

For the horizontal turbulent viscosity, we used two different prescriptions:

$$\nu_h = r \sqrt{[Cr\overline{\Omega}|2V_2 - \alpha U_2|]} \quad \text{where } \alpha = \frac{1}{2} \frac{\partial \ln(r^2 \overline{\Omega})}{\partial \ln r}, \quad (29)$$

after Mathis et al. (2004), and

$$\nu_h = \frac{r}{C_H} |2V_2 - \alpha U_2| \quad (30)$$

after Zahn (1992). Here the parameter $C = 1.6 \times 10^{-6}$, and C_H is a parameter of order unity, and V_2 is given by Eq. (5). As for the vertical turbulent diffusion coefficient, we assume that $D_h \simeq \nu_h$.

We stress that the advective character of the transport of angular momentum by the meridional circulation makes the interpretation of the whole hydrodynamics more complex than when the diffusive approximation is used (e.g., Endal & Sofia 1978; Pinsonneault et al. 1989; Heger et al. 2000). This is one of the reasons we developed the tools that we describe in the following section.

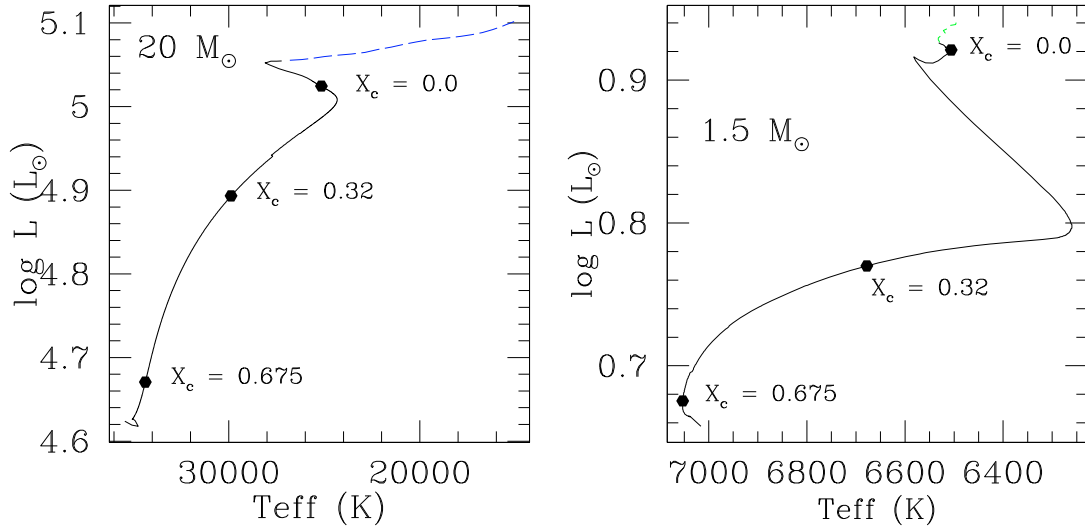


Fig. 2. Evolutionary path in the HR diagram of a $20 M_{\odot}$ (left panel) and $1.5 M_{\odot}$ (right panel) star with solar composition. The solid line represents the main sequence. The dots on each plot indicate specific locations where a detailed analysis of the structure is presented.

3. Numerical simulation of secular transport

In this section, we apply the formalism described in Sect. 2 to the evolution of rotating stars with initial masses of 20 and $1.5 M_{\odot}$ and metallicity close to solar value ($Z = 0.017$ and 0.02 for the $20 M_{\odot}$ and the $1.5 M_{\odot}$ respectively). In the Hertzsprung-Russell diagram shown in Fig. 2, the black dots indicate the evolutionary points where a snapshot on the internal structure will be taken and analysed in detail. These points are associated with central hydrogen mass fractions $X_c = 0.675$, 0.32 , 0.00 as indicated on the tracks.

A number of results for the hydrodynamics of such rotating models have already been published (Talon 1997; Talon & Charbonnel 1998; Meynet & Maeder 2000; Palacios et al. 2003; Mathis et al. 2004; Palacios et al. 2006; Decressin et al. 2007), and we rely on this experience to prove the relevance of the diagnosis tools that we have developed. The models presented here were computed with the stellar evolution code STAREVOL V2.90, and the reader is referred to Siess et al. (2000), Palacios et al. (2006), and Siess (2006) for a detailed description of the input physics. We simply recall the main characteristics and parameters used for the modelling.

The reference solar composition we use follows Grevesse et al. (1996). The standard mixing length theory is used to model the temperature gradient in the convection zones and the parameter $\alpha_{\text{MLT}} = 1.75$. The atmosphere is treated in the gray approximation and integrated up to an optical depth $\tau \approx 5 \times 10^{-3}$.

In both simulations, mass loss is included from the zero age main sequence on. We use the Reimers (1975) prescription for the low-mass star, with a parameter $\eta_{\text{R}} = 0.5$ (see also Palacios et al. 2006) and the prescriptions by Vink et al. (2000) for the massive star. Rotation effects on mass loss are accounted for following Maeder & Meynet (2001). Angular momentum losses associated with mass loss are also accounted for, but their anisotropy (Maeder 2002) is not included in the computations.

For the transport of angular momentum and nuclides, we use Eq. (29) as the prescription for D_h for the $20 M_{\odot}$ model. For the $1.5 M_{\odot}$ model, we use Eq. (30) as in Palacios et al. (2003) who shows that it yields to a very good agreement with the surface velocity and the light nuclides (Li, Be) surface abundances that are observed in open clusters such as the Hyades. The expression for the vertical turbulent diffusion coefficient is given by Eq. (28)

in both models. For the transport of nuclides, we do not account for atomic diffusion.

In our framework, the evolution of the angular velocity profile and of the meridional circulation in the radiative zones is governed by a system of five first-order partial differential equations. These equations are obtained by splitting Eq. (11) into first-order equations that are complemented by Eqs. (17) and (27). We use a Newton-Raphson relaxation method (Heyney et al. 1964) to solve these equations. In convection zones we assume solid-body rotation ($\Omega(r) = \text{cst}$) and do not solve the aforementioned system. The boundary conditions at the radiative zone limits are the same as those described in Palacios et al. (2003).

We choose initial velocities on the ZAMS that reflect an average velocity for main sequence B and F stars (Fukada 1982; Abt et al. 2002; Gaigé 1993). The adopted initial velocity on the ZAMS are $v_{\text{ZAMS}} = 300 \text{ km s}^{-1}$ and $v_{\text{ZAMS}} = 100 \text{ km s}^{-1}$ for the $20 M_{\odot}$ and the $1.5 M_{\odot}$, respectively.

The evolution of the surface velocity can be affected by the magnetic torques exerted at the surface of the star during its early evolution (Schatzman 1962). This magnetic braking is generally associated with the presence of a convective envelope; it will thus only be applied to the low-mass star model, following Kawaler's (1988) formalism as described in Palacios et al. (2003). In the case of massive stars, it is only very recently that magnetic fields have been detected in normal O and B stars, and they appear to be very weak or nonexistent (Bouret et al. 2008; Schnerr et al. 2008). Moreover, O and B stars with measured $v \sin i$ appear to be fast rotators. For these reasons, we have decided not to account for magnetic braking in the $20 M_{\odot}$ model.

In the following sections, we present new diagnosis tools to better understand and quantify the processes responsible for the building up of differential rotation in stellar interiors.

3.1. Rotational profiles and differential rotation

3.1.1. $20 M_{\odot}$ model

The $20 M_{\odot}$ model does not undergo magnetic braking and thus remains a fast rotator during its main sequence (MS) evolution, with $v_{\text{surf}} \approx 250 \text{ km s}^{-1}$. Similarly to what was obtained by Meynet & Maeder (2000), differential rotation rapidly develops in the interior, as firsts meridional flow transports angular

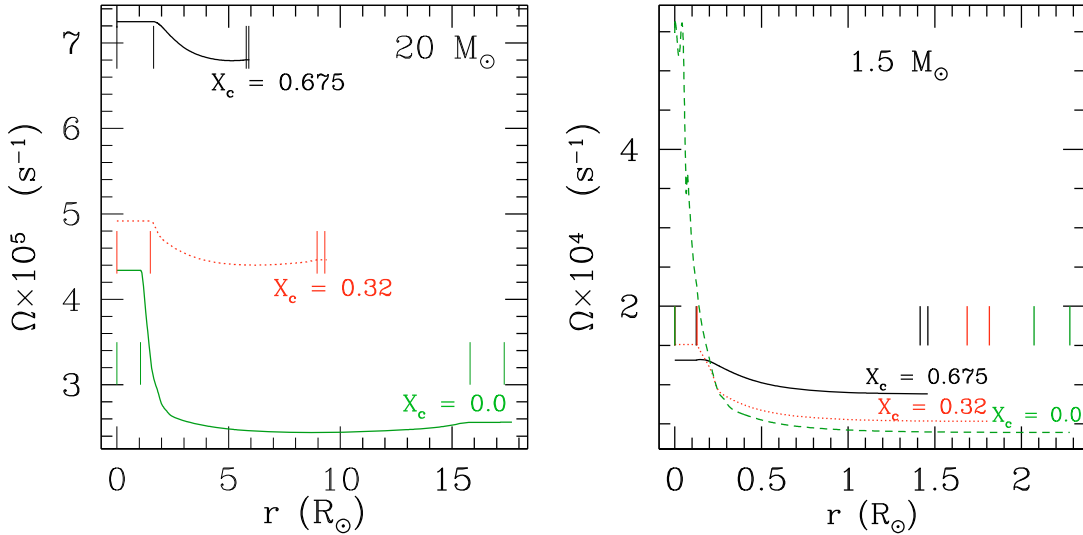


Fig. 3. Angular velocity profile inside the $20 M_{\odot}$ (left panel) and $1.5 M_{\odot}$ (right panel) model as a function of the (expanding) radius, at three different evolutionary stages on the main sequence, as indicated by the central hydrogen content. The short vertical lines indicate the location of the convection zones. In the $1.5 M_{\odot}$ model, at the end of the main sequence ($X_c = 0$), the convective core has disappeared.

momentum inwards. After a transient phase that lasts ~ 1 Myr following the arrival on the ZAMS, the morphology of the rotation profile is not significantly affected until the star reaches the turn-off, as shown in Fig. 3 (left panel).

Above the radial coordinate $5 R_{\odot}$ (resp. $6 R_{\odot}$ and $10 R_{\odot}$) for $X_c = 0.675$ (resp. $X_c = 0.32$ and $X_c = 0.0$), the angular velocity gradient becomes positive due to very efficient transport of angular momentum by the meridional circulation in a region where the density is low (see Sect. 3.2). This inversion of the angular velocity gradient should be counteracted by the shear turbulence that tends to smooth out this profile. However, the shear can only operate if the flow is turbulent, i.e., if the Reynolds condition $\nu_V \geq \nu \text{Re}_c$ is satisfied where $\text{Re}_c \approx 1$ is the critical Reynolds number and ν_V and ν the shear and microscopic viscosities, respectively. Below the convective envelope (where $\partial_r \bar{\Omega} \approx 0$), this condition is not fulfilled, and the shear is unable to connect the region with positive angular velocity gradient with the one where $\partial_r \bar{\Omega} = 0$ (see the dip in the profile of D_v in Fig. 15). This explains the persistence of this positive gradient. Computations done without taking into account the Reynolds criterion show that this positive gradient is reduced (by a factor 3 to 5) but is still present, although at a lower level. It should be noted that this inversion has already been obtained by Talon et al. (1997) in the asymptotic regime for a $9 M_{\odot}$ with an equatorial angular velocity of 425 km s^{-1} . This feature can be linked to the Gratton-Öpik term in the meridional circulation (see Sect. 3.4.1).

The decrease in the angular velocity during the MS evolution is due to two factors: (1) mass and angular momentum losses by the stellar winds and (2) structural changes that lead to an overall expansion of the star. It should be noted, however, that up to the point where $X_c \approx 0.1$, the contrast in Ω between the centre and the surface is small, not exceeding 20% .

3.1.2. $1.5 M_{\odot}$ model

In contrast to the $20 M_{\odot}$ star, the $1.5 M_{\odot}$ star undergoes magnetic braking at its arrival on the ZAMS, resulting in a strong extraction of angular momentum, as shown in Talon & Charbonnel (1998) and Palacios et al. (2003, 2006). During the first 800 Myr, the surface equatorial velocity drops from

100 km s^{-1} to 78 km s^{-1} , in agreement with observations in open clusters like the Hyades (i.e., Gaigé 1993). Beyond this point, the braking becomes less efficient and the surface rotational velocity continues to decrease slowly until the star reaches the turn-off with $v_{\text{surf}} \approx 53 \text{ km s}^{-1}$ at age 2.35 Gyr.

The right panel of Fig. 3 presents the evolution of the angular velocity profile on the MS. When $X_c = 0.675$, i.e. when the star is ~ 200 Myr old, the core already rotates 1.5 times faster than the surface. While the angular velocity in the convective core slowly increases, the extraction of angular momentum at the surface slows down the surface layers and differential rotation increases during the MS. When the convective core disappears at central H-exhaustion, the contraction of the inner shells produces a much steeper Ω -gradient (right panel, Fig. 3) with $\Omega_{\text{centre}} = 14 \times \Omega_{\text{surf}}$.

3.2. Meridional circulation

In this section, we isolate the processes that are at the origin of meridional circulation.

3.2.1. $20 M_{\odot}$ model

Figure 4 shows the meridional flows in the radiative interior of the $20 M_{\odot}$ when the central hydrogen mass fraction reaches $X_c = 0.32$. They are represented in terms of the stream function $\xi_M(r, \theta)$ (see Eq. (8)). The circulation consists of a single counterclockwise loop, by which matter is transported inward along the rotational axis, and is conveyed outward in the equatorial plane. These flows thus extract angular momentum from the deep interior to the surface. Matter is conserved in the meridional circulation currents and $\bar{\rho} \|\mathbf{U}_M\| = \text{constant}$ along the flux lines (shown in Fig. 4). The abrupt jump in density occurring near the surface produces an increase in the meridional circulation velocity as illustrated by Fig. 5. This in turn forces the inversion of the angular velocity gradient mentioned in Sect. 3.1 via the Gratton-Öpik term ($\propto -\bar{\Omega}^2 / 2\pi G \bar{\rho}$, see Eq. (B.1) in Appendix B). The velocities are maximum in the low-density regions (i.e. below the surface) where they reach $\|\mathbf{U}_M(r, \theta)\| \approx 1.6 \text{ m s}^{-1}$.

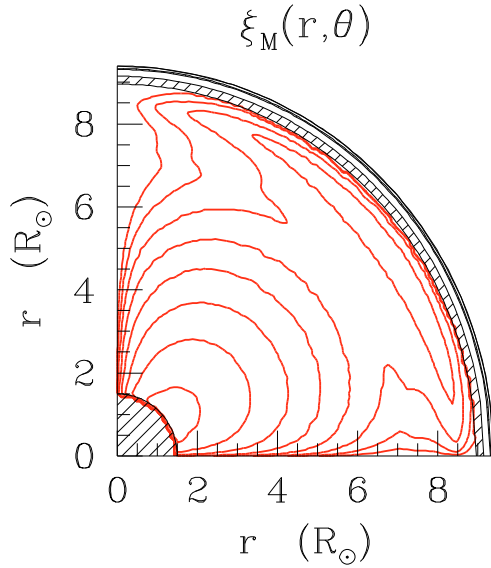


Fig. 4. Meridional circulation currents in the $20 M_{\odot}$ model when $X_c = 0.32$. Solid thin (red) lines indicate counterclockwise circulation ($U_2 < 0$), which carries angular momentum outwards. Hatched regions correspond to convection zones.

After a short adjustment phase, which depends on the initial conditions that have been imposed on the ZAMS (uniform rotation), the meridional circulation settles into a counterclockwise regime, as was noticed by [Meynet & Maeder \(2000\)](#). This flow thus carries angular momentum outwards, in order to compensate for the structural changes, i.e. the inflation of the envelope and the contraction of the core.

Figure 5 shows the a posteriori reconstruction of the meridional circulation based on the integration of the equation for the evolution of angular momentum (Eq. (16)), at $X_c = 0.32$. U_{Γ} represents the angular momentum extraction and U_V what is due to the shear. In the inner part of the radiative zone, below $7 R_{\odot}$, the meridional circulation is powered by the extraction of angular momentum, as $|U_{\Gamma}| \gg |U_V|$. Near the surface, U_V becomes negative and the same order as U_{Γ} . This inversion of U_V is correlated with the sign change of the angular velocity gradient since $U_V = -5v_r \partial_r \ln \bar{\Omega}$. U_{Γ} may be considered as a measure of the departure from a stationary regime, where angular momentum transport by shear (U_V) and meridional circulation (U_2) compensate for each other. This balance is barely achieved in the uppermost part of the star (above $8 R_{\odot}$), but the bulk of the radiative interior is not in a stationary state, as already pointed out in [Talon et al. \(1997\)](#) and [Meynet & Maeder \(2000\)](#) on the basis of an asymptotic analysis. Here, we confirm this result but also track down the importance of the shear versus angular momentum transport in shaping the meridional circulation.

3.2.2. $1.5 M_{\odot}$ model

The wind-driven meridional flows are depicted in Fig. 6 for the low-mass star at the three evolutionary stages indicated in Fig. 2. Compared to the $20 M_{\odot}$ model, the topology of the meridional circulation is more complex. In panels 1 and 3, the circulation presents two loops: a small clockwise loop in the central regions and a large counterclockwise loop connecting the interior to the surface. As in the massive star model, the counterclockwise loop carries angular momentum outward and is driven by the strong extraction of angular momentum (here largely due to the

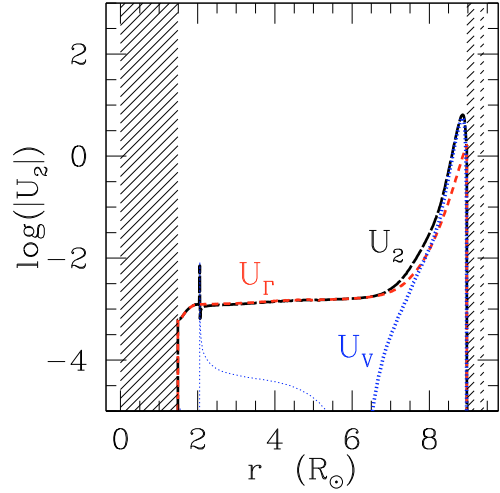


Fig. 5. Decomposition of the meridional circulation based on the equation of angular momentum evolution in the $20 M_{\odot}$ star, when $X_c = 0.32$. Hatched regions correspond to convection zones. U_{Γ} (short-dashed red line, see Eq. (16)), U_2 (meridional circulation, in long-dashed black line), and U_V (turbulent transport, in dotted blue line) are presented on a logarithmic scale. The thin part of the curves means that the plotted quantity is positive and the bold parts that it is negative.

magnetic braking). The clockwise loop corresponds to matter flowing from the equator to the pole, which results in deposition of angular momentum in this region. Such loops appear only in the centre and do not persist over the whole evolution on the main sequence.

At the beginning of the MS evolution, the meridional circulation velocity is maximal in a thin layer below the surface as a result of the applied magnetic torque. The amplitude of the meridional circulation velocity $\|U_2\|$ does not exceed 0.5 m s^{-1} at its maximum and is approximately of 10^{-4} in the bulk of the radiative zone. As the star spins down, the braking becomes less efficient and the meridional circulation weakens by 3 orders of magnitude. The large difference in meridional velocity between the low-mass and the massive star is due to the L/M factor (Eq. (18)), which increases with stellar mass, and to the higher initial angular velocity of the $20 M_{\odot}$ star.

Figure 7 is similar to Fig. 5 but for the 3 models selected during the MS evolution of the $1.5 M_{\odot}$ star. As for the $20 M_{\odot}$ model, the meridional circulation is driven by the local loss of angular momentum (U_{Γ} term that matches the U_2 profile), the contribution of the vertical shear (U_V) being always much smaller, except in the central regions where it can be about U_{Γ} . This figure confirms that the inward transport of angular momentum (clockwise meridional circulation loops) is associated with a positive value of U_{Γ} , corresponding to a local gain of angular momentum (see Eq. (16)). In most of the radiative zone, $U_V \ll U_2$, and contrary to what was found in the massive star model, the circulation in the upper part of the radiative zone never approaches the stationary regime. As shown by [Talon et al. \(1997\)](#), the extraction of angular momentum by magnetic braking together with the very small meridional velocities prevent the inversion of the angular velocity gradient in the regions of low density as was the case in the massive star model. Consequently, $U_V \propto -\partial_r \bar{\Omega}$ always remains positive. Besides, during the main sequence the differential rotation remains too small to ensure an efficient transport of angular momentum by the shear turbulence.

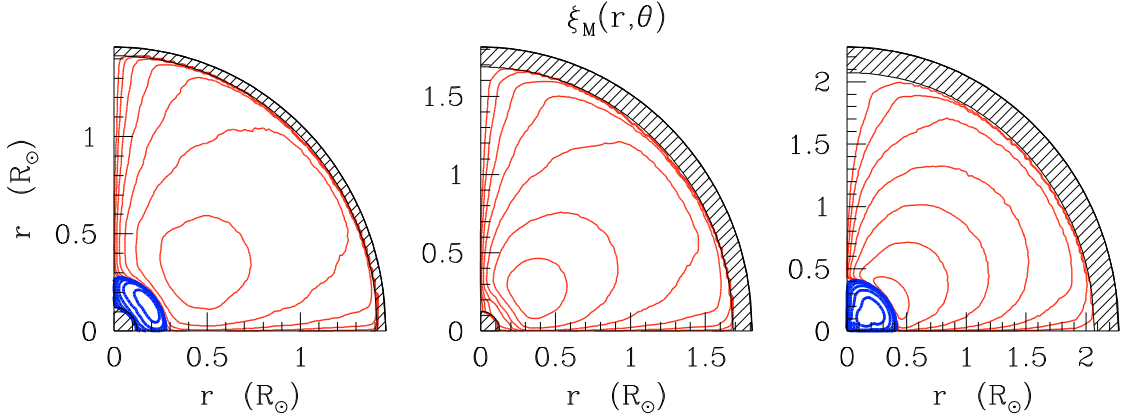


Fig. 6. Meridional circulation flow in the $1.5 M_{\odot}$ model when $X_c = 0.675$ (left panel), 0.32 (middle panel), and 0.0 (right panel). Solid thin (red) lines indicate counterclockwise circulation ($U_2 < 0$) and solid bold (blue) lines clockwise circulation ($U_2 > 0$). In this model, the outer cell is turning counterclockwise allowing the extraction of angular momentum by the wind. Hatched regions indicate convection zones.

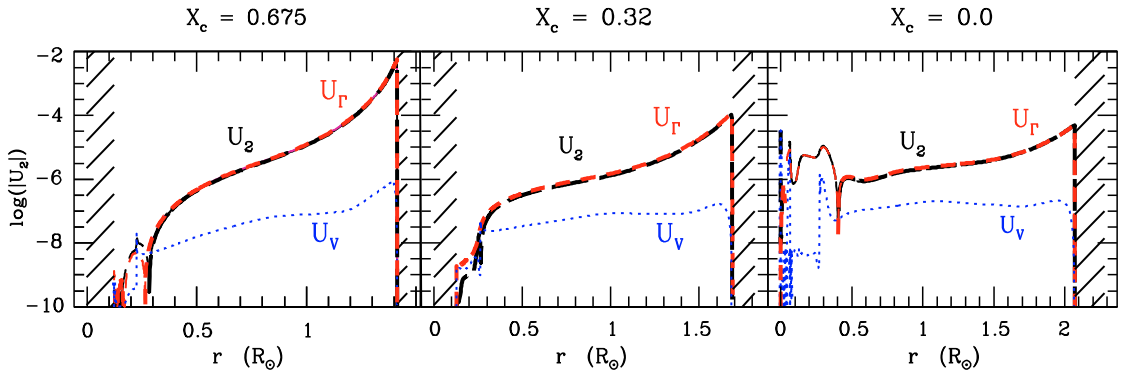


Fig. 7. Decomposition of the vertical component of the meridional circulation U_2 according to Eq. (16) for the $1.5 M_{\odot}$ model at the three different epochs indicated on top of each panel. The term due to angular momentum transport, U_r , is shown by a dashed red line, the one due to vertical shear, U_v , is by a dotted blue line. The value of U_2 obtained in the simulation is indicated by a long-dashed black line. Thin and thick lines respectively represent positive and negative values.

3.3. Angular momentum transport

In Sect. 3.2 we already compared the respective contributions of meridional circulation and turbulence in the transport of angular momentum, in agreement with results from the literature. We now examine the problem from a different perspective, based on the fluxes carried by the two processes (Eq. (12)).

3.3.1. $20 M_{\odot}$ model

Figure 8 shows the two components of the angular momentum flux associated with the meridional circulation and shear. In this model the meridional circulation presents only one counterclockwise loop so the transport occurs in the same direction in the whole radiative zone and carries angular momentum from the core to the surface ($F_{MC} > 0$). Below $r = 6 R_{\odot}$ the turbulent shear works in the same direction ($F_S > 0$), but its contribution is negligible compared to that of the meridional circulation. Above $6 R_{\odot}$, the angular velocity gradient changes sign and shear takes over the advection of angular momentum.

Both F_S and F_{MC} are of opposite sign below the convective envelope during the MS evolution and grow in amplitude due to the radial expansion of the outer low-density layers (see Eqs. (13) and (14)). This configuration tends to impose a stationary circulation in this region. On the other hand, these fluxes have the same sign deeper in the interior and act jointly to

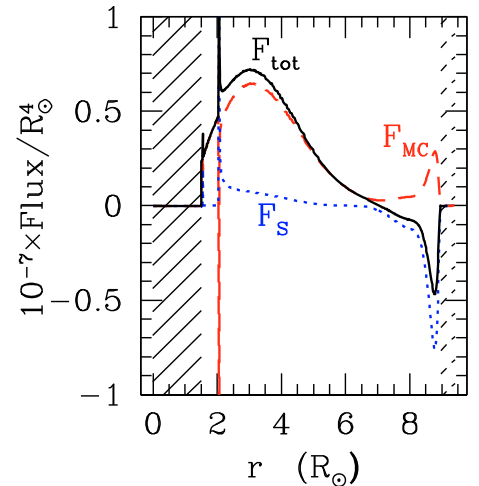


Fig. 8. The total flux of angular momentum (solid black line) decomposed into its meridional circulation $F_{MC}(r) = -\frac{1}{5}\bar{\rho}r^4\bar{\Omega}U_2$ (dashed red line) and turbulence $F_S(r) = -\bar{\rho}v_r r^4 \partial_r \bar{\Omega}$ components (dotted blue line) for the $20 M_{\odot}$ model when $X_c = 0.32$. The fluxes are rescaled by R_{\odot}^4 .

compensate for the structural changes of the star by redistributing the total angular momentum.

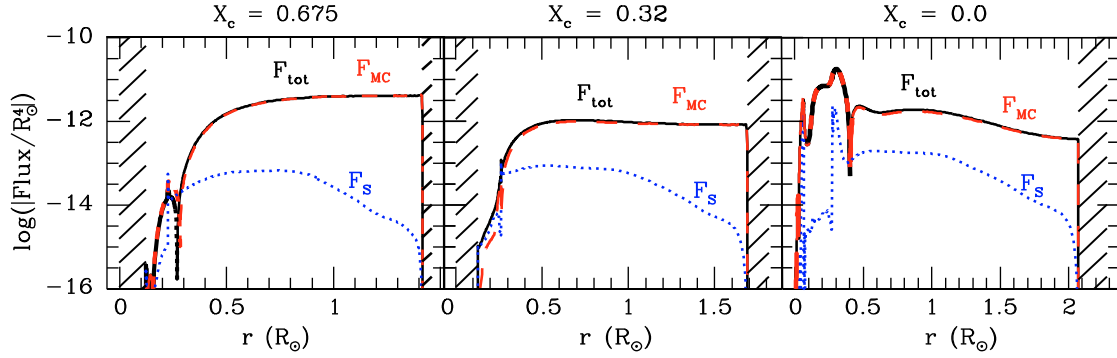


Fig. 9. Same as Fig. 8 for the $1.5 M_{\odot}$ model at the three selected evolutionary stages indicated by X_c . In this graph, the logarithm of the absolute value of the flux is plotted and rescaled by R_{\odot}^4 . Thin and bold lines represent positive and negative fluxes, respectively.

3.3.2. $1.5 M_{\odot}$ model

In the low-mass model, the meridional circulation dominates the angular momentum transport and $F_{MC} \approx F_{Tot}$ at all times on the main sequence (Fig. 9). The bold parts of the curves indicate positive, outward fluxes that are associated with the counterclockwise meridional currents described in Fig. 6.

Unlike in the massive star model, shear extracts angular momentum everywhere because of the monotonous decrease in Ω with radius. Nevertheless, its contribution remains negligible. At the turn-off, the meridional circulation and angular velocities have dropped in the outer parts of the radiative zone because of the braking of the surface layers and structural changes. This weakens F_{MC} , while F_S remains almost unaltered. In the central regions, both Ω and $\partial_r \Omega$ substantially increase leading to a concomitant rise in F_{MC} and F_S . The increase and sign change in F_{MC} between $r = 0.05 R_{\odot}$ and $r = 0.4 R_{\odot}$ is partly due to the off-centre displacement of the nuclear energy production region when H is exhausted in the core.

In summary, our diagnostic tools applied on two well-known cases allow us to give quantitative estimates for the main properties of angular momentum transport already discussed in the literature (see e.g., Meynet & Maeder 2000; Palacios et al. 2003). In low-mass stars, angular momentum transport is ensured by meridional currents that are primarily generated by the action of the applied torques resulting from the action of magnetic braking. In the massive star, owing to the differences in structure (density stratification, radius) and in surface velocities, the gradient of angular velocity becomes positive in the outer layers of the star, and there shear turbulence takes over the transport of angular momentum.

3.4. Thermal relaxation

Let us now analyse how thermal relaxation is achieved, as described by the heat Eq. (18), which rules the temperature perturbations. As explained previously, the meridional circulation is mainly driven by the extraction of angular momentum due to angular momentum losses at the surface (i.e. by the external torques) and to structural readjustments (such as the expansion of the star on the MS). This circulation advects specific entropy, which perturbs the thermal equilibrium and induces temperature fluctuations described by Ψ_2 . These are linked to the differential rotation through the baroclinic Eq. (17), so that the heat equation is actually tightly coupled with the equation of angular momentum transport (11). We examine how this works in our models.

3.4.1. $20 M_{\odot}$ model

Each term of Eq. (19) is represented in Fig. 10 (left panel). The plot is separated into two panels, the upper and lower ones showing the positive and negative parts of each profile respectively, on a logarithmic scale. The differential rotation adjusts itself so that the advection of entropy by the meridional circulation ($\tilde{\mathcal{T}}_{Adv}$) is almost exactly compensated for by the thermal readjustment via the barotropic ($\tilde{\mathcal{T}}_B$) and thermic ($\tilde{\mathcal{T}}_{Th}$) terms. The other terms, associated with the non-stationarity ($\tilde{\mathcal{T}}_{NS}$) and with the nuclear and gravitational energy generation ($\tilde{\mathcal{T}}_{N-G}$), are several orders of magnitude smaller and thus can be neglected during the main sequence evolution. From this simplification, splitting the divergence of the radiative flux (third term on the right hand side of Eq. (18)) into barotropic and thermic (baroclinic) components thus appears to be somewhat artificial.

The temperature perturbations Ψ_2 quickly relax to the asymptotic regime, which involves only the source ($\tilde{\mathcal{T}}_{Adv}$) and diffusion ($\tilde{\mathcal{T}}_B + \tilde{\mathcal{T}}_{Th}$) terms (see also Appendix B for description of these terms), and Eq. (18) gives

$$\nabla \cdot (\chi \nabla T) - \nabla \cdot F_H \approx -\bar{\rho} \bar{T} U_r \partial_r \bar{S} \quad (31)$$

and

$$\tilde{\mathcal{T}}_{2,B} + \tilde{\mathcal{T}}_{2,Th} \approx \bar{\rho} \bar{T} C_p \frac{N_T^2}{g \delta} U_2. \quad (32)$$

To explicitly disentangle the role played by each component in shaping the entropy transport, we split the barotropic term as

$$\tilde{\mathcal{T}}_B = \tilde{\mathcal{T}}_{B1} + \tilde{\mathcal{T}}_{B2} + \tilde{\mathcal{T}}_{B3} + \tilde{\mathcal{T}}_{B4}, \quad (33)$$

where

$$\tilde{\mathcal{T}}_{B1} = \bar{\rho} \frac{L}{M} \frac{2}{3} \left(1 - \frac{\bar{\Omega}^2}{2\pi G \bar{\rho}} \right) \bar{\Omega}^2 \partial_r \left(\frac{r^2}{g} \right), \quad (34)$$

$$\tilde{\mathcal{T}}_{B2} = -\bar{\rho} \frac{L}{M} \frac{4}{9} \frac{\rho_m}{\bar{\rho}} (\varphi \Lambda_2 - \delta \Psi_2) \bar{\Omega}^2 \partial_r \left(\frac{r^2}{g} \right), \quad (35)$$

$$\tilde{\mathcal{T}}_{B3} = -\bar{\rho} \frac{L}{M} \frac{2}{3} \frac{(\bar{\epsilon} + \bar{\epsilon}_{grav})}{\epsilon_m} \bar{\Omega}^2 \partial_r \left(\frac{r^2}{g} \right), \quad (36)$$

and

$$\tilde{\mathcal{T}}_{B4} = -\bar{\rho} \frac{L}{M} \frac{2}{3} \frac{\rho_m}{\bar{\rho}} (\varphi \Lambda_2 - \delta \Psi_2). \quad (37)$$

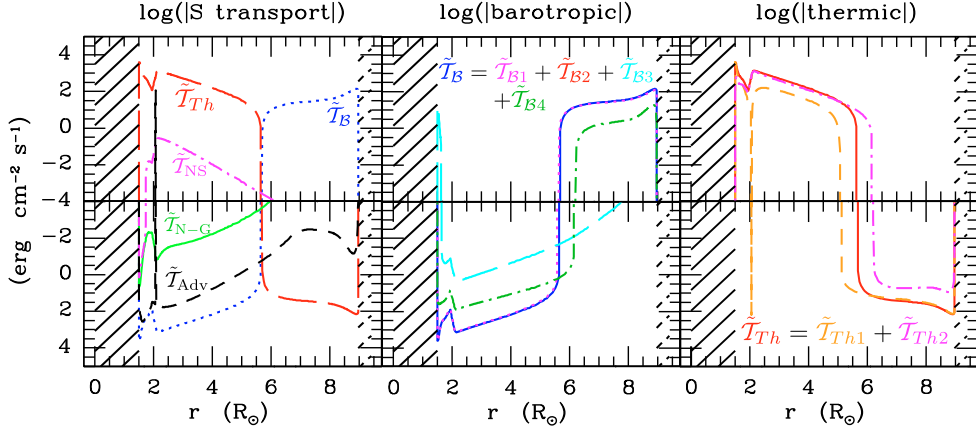


Fig. 10. Representation of the different components of the heat equation (Eq. (18)) for the $20 M_{\odot}$ model when $X_c = 0.32$ (left panel). The upper panel shows $\log|S|$ for $S > 0$, while the lower panel shows $\log|S|$ for $S < 0$. Shown are the non-stationary (NS, dot long-dashed magenta line), barotropic (B, dotted blue line), baroclinic (Th long-dashed red line), advective (dashed black line) terms, and the contribution due to the nuclear and gravitational energy variations (N-G, solid green lines). The central panel shows the components of the barotropic term: \tilde{T}_B (solid line), \tilde{T}_{B1} (dotted line), \tilde{T}_{B2} (long-dashed line), \tilde{T}_{B3} (dotted-dashed line). The right panel shows the thermic components: \tilde{T}_{Th} (solid), \tilde{T}_{Th1} (dashed line), and \tilde{T}_{Th2} (dotted line).

Here, \tilde{T}_{B1} represents the “pure” barotropic term (which does not depend on $\partial_r \bar{\Omega}$), while \tilde{T}_{B2} and \tilde{T}_{B3} are the first and second baroclinic corrections due to the differential rotation (cf. Eq. (17)). Finally, \tilde{T}_{B3} is associated with the energy production on the isobar.

Next, the thermic term is decomposed as

$$\tilde{T}_{Th} = \tilde{T}_{Th1} + \tilde{T}_{Th2}, \quad (38)$$

where

$$\tilde{T}_{Th1} = -\bar{\rho} \frac{L}{M} \left(\frac{\rho_m r}{\bar{\rho}} \frac{1}{3} \partial_r \mathcal{A}_2(r) - \frac{2H_T}{3r} \Psi_2 \right), \quad (39)$$

and

$$\tilde{T}_{Th2} = -\bar{\rho} \frac{L}{M} \frac{2H_T}{3r} \frac{D_h}{K_T} \Psi_2. \quad (40)$$

The term \tilde{T}_{Th1} comes from the diffusive Laplacian acting on Ψ_2 , while \tilde{T}_{Th2} is related to the heat flux carried by the horizontal turbulence ($\nabla \cdot \mathbf{F}_H$).

Middle and left panels of Fig. 10 display these components for the barotropic (\tilde{T}_B) and thermic (\tilde{T}_{Th}) terms. We first note that the behaviour of \tilde{T}_B closely follows that of \tilde{T}_{B1} . This result is expected, as the terms \tilde{T}_{B2} and \tilde{T}_{B3} are driven by the T- and μ -fluctuations, which remain small in main sequence stars (see below). Moreover the term \tilde{T}_{B3} scales with $(\bar{\epsilon} + \bar{\epsilon}_{\text{grav}})/\epsilon_m$ (i.e., the ratio of energy production at a given radius with respect to the total energy enclosed in the sphere of this radius), which remains small as the (nuclear) energy production is mainly located in the convective core. It should also be noted that the relative strength of the two baroclinic corrections scales with $\bar{\Omega}^2 \partial_r \left(\frac{r^2}{g} \right)$, which is always very small (between 10^{-14} and 10^{-10} in the whole radiative region and mainly varies via the $\bar{\Omega}^2$ dependence). This explains why the term \tilde{T}_{B2} does not appear in Fig. 10 (middle panel) and can be neglected during the main sequence evolution.

The thermic term (\tilde{T}_{Th}) requires more attention as no specific component dominates in the whole radiative layer. Below the surface and above the convective core the term \tilde{T}_{Th1} dominates while \tilde{T}_{Th} is driven by \tilde{T}_{Th2} in the centre of the radiative zone. As discussed in the next section, this result strongly depends on the D_h/K_T ratio.

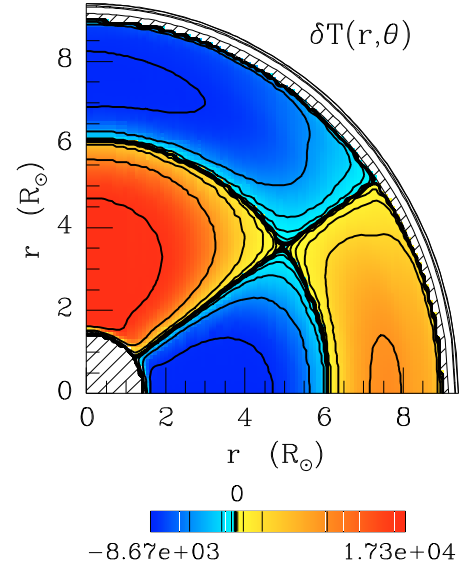


Fig. 11. Two-dimensional reconstruction of the temperature fluctuations $\delta T = \bar{T} \Psi_2 P_2(\cos \theta)$ in the $20 M_{\odot}$ model when $X_c = 0.32$. The light (blue) parts are for negative fluctuations and the darker (red) are for positive ones.

Figure 11 presents the two-dimensional reconstruction of the temperature perturbations in the meridional plane, i.e. $\delta T(r, \theta) = \bar{T}(r) \Psi_2(r) P_2(\cos \theta)$. These are directly connected to the behaviour of $\bar{\Omega}$ -gradient: the temperature is higher at the poles (closer to the rotational axis) than at the equator where $\partial_r \bar{\Omega} < 0$, i.e. where the angular velocity decreases with increasing radius. Near the surface, the situation is reversed since $\partial_r \bar{\Omega}$ is positive there.

3.4.2. $1.5 M_{\odot}$ model

Figure 12 is similar to Fig. 10 for the $1.5 M_{\odot}$ model, but contrary to the $20 M_{\odot}$ model, \tilde{T}_{Adv} is now the same order of magnitude as \tilde{T}_B and \tilde{T}_{Th} . This is because magnetic braking forces a larger extraction of angular momentum. Let us note that the reversal of the meridional circulation shown in Figs. 6 and 7 is proven

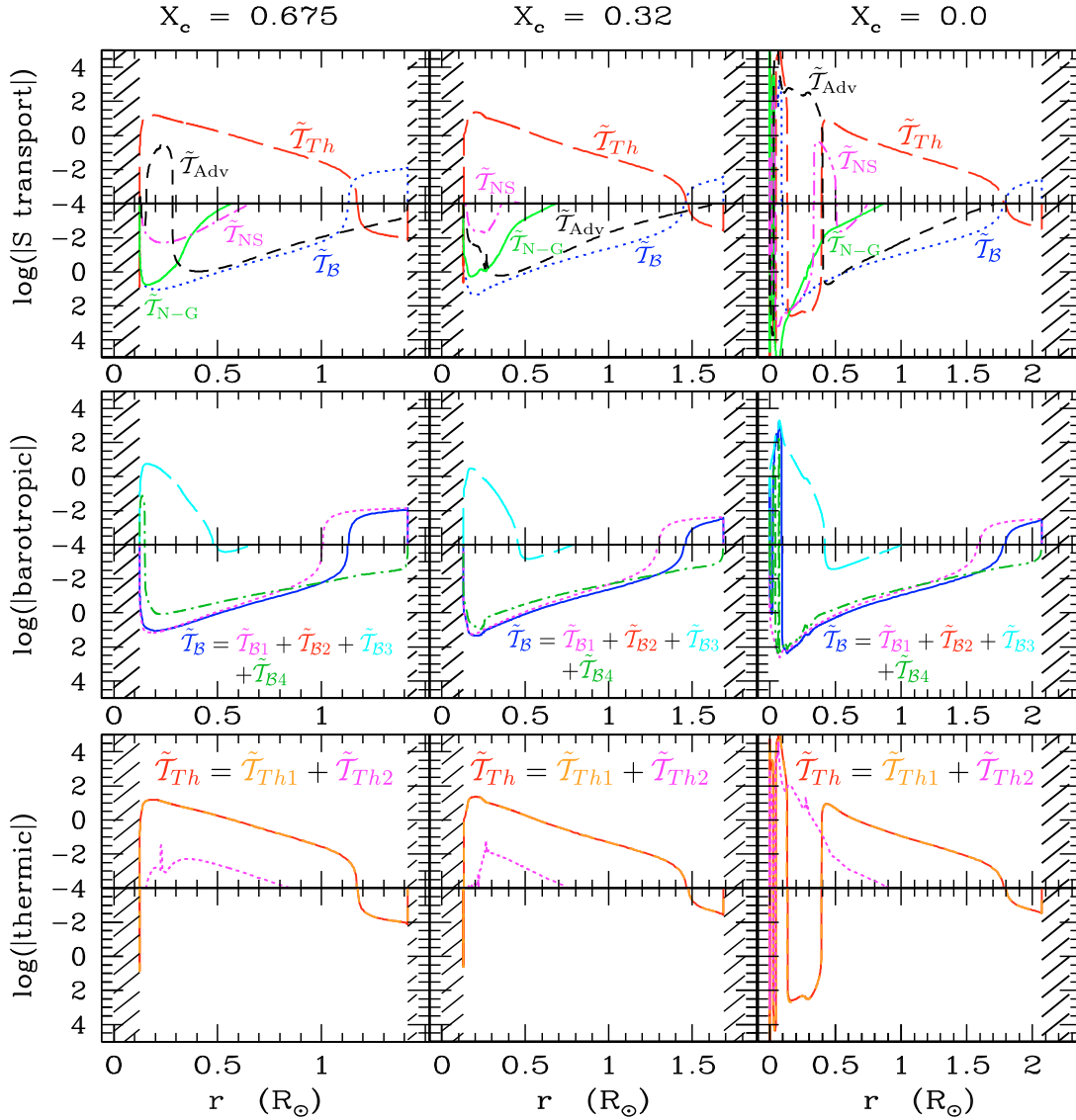


Fig. 12. Same as Fig. 10 for the $1.5 M_{\odot}$ model at the three evolutionary points indicated by X_c . All quantities are shown in $\text{erg cm}^{-2} \text{s}^{-1}$.

by the sign change of $\tilde{\mathcal{T}}_{\text{Adv}}$. Also in contrast to the massive star, the nuclear and gravitational term, $\tilde{\mathcal{T}}_{\text{N-G}}$, becomes comparable to the advective one near the convective core, and should thus not be neglected. Finally, except near turn-off where it becomes important in the interior, the non-stationary term, $\tilde{\mathcal{T}}_{\text{NS}}$, is generally several orders of magnitudes smaller than the other terms during most of the main sequence.

Equation (19) is thus left with four terms balancing each other. The thermic (baroclinic) and barotropic terms have similar amplitudes and opposite signs and their sum balances the sum of the advective term and the nuclear and gravitational heating:

$$\tilde{\mathcal{T}}_{\mathcal{B}} + \tilde{\mathcal{T}}_{\text{Th}} \approx \tilde{\mathcal{T}}_{\text{adv}} + \tilde{\mathcal{T}}_{\text{N-G}}. \quad (41)$$

We finally note that this situation is no longer valid at the turn-off as seen in the third column of Fig. 12. There, the non-stationary terms become dominant in the deep interior and must not be neglected anymore for the following evolutionary phase.

Figure 12 also displays the components of the barotropic and thermic term in the same way as in Fig. 10. In most of the radiative interior, $\tilde{\mathcal{T}}_{\mathcal{B}}$ follows the barotropic component, $\tilde{\mathcal{T}}_{\mathcal{B}1}$, except below the surface where the contribution of the second baroclinic correction $\tilde{\mathcal{T}}_{\mathcal{B}4}$ becomes relevant. As in the $20 M_{\odot}$ model,

$\tilde{\mathcal{T}}_{\mathcal{B}3}$ is negligible during the main sequence. However, in the last model ($X_c = 0.0$), this term dominates in the centre due to the release of (a) nuclear energy by the hydrogen-burning shell and (b) gravitational energy by the contracting core.

In contrast to the $20 M_{\odot}$, the heat diffusion, $\tilde{\mathcal{T}}_{\text{Th}2} (\propto D_h/K_T)$, plays no role in the thermic term, $\tilde{\mathcal{T}}_{\text{Th}}$, which is solely driven by the Laplacian component, $\tilde{\mathcal{T}}_{\text{Th}1}$. The $1.5 M_{\odot}$ model has been computed with the Zahn (1992) prescription for the horizontal turbulent diffusion coefficient D_h leading to $D_h/K_T \approx 10^{-4} - 10^{-3}$, whereas this ratio amounts to about 10 for the $20 M_{\odot}$, where the Mathis et al. (2004) prescription was used (see Sect. 3.5). At the centre of the last shown model, the Laplacian component presents a very complex behaviour as it is sensitive to the first, second, and third radial derivatives of $\bar{\Omega}$. Figure 3 reveals that the profile of $\bar{\Omega}$ presents some rapid variations in this region which explain this intricate feature.

Figure 13 displays the temperature fluctuations that essentially follow the gradient of $\bar{\Omega}$ as in the $20 M_{\odot}$ case. The main difference is due to the presence of a second circulation loop. The amplitude of the fluctuations remains globally of the same while the star is on the MS, and amount to about a few percent.

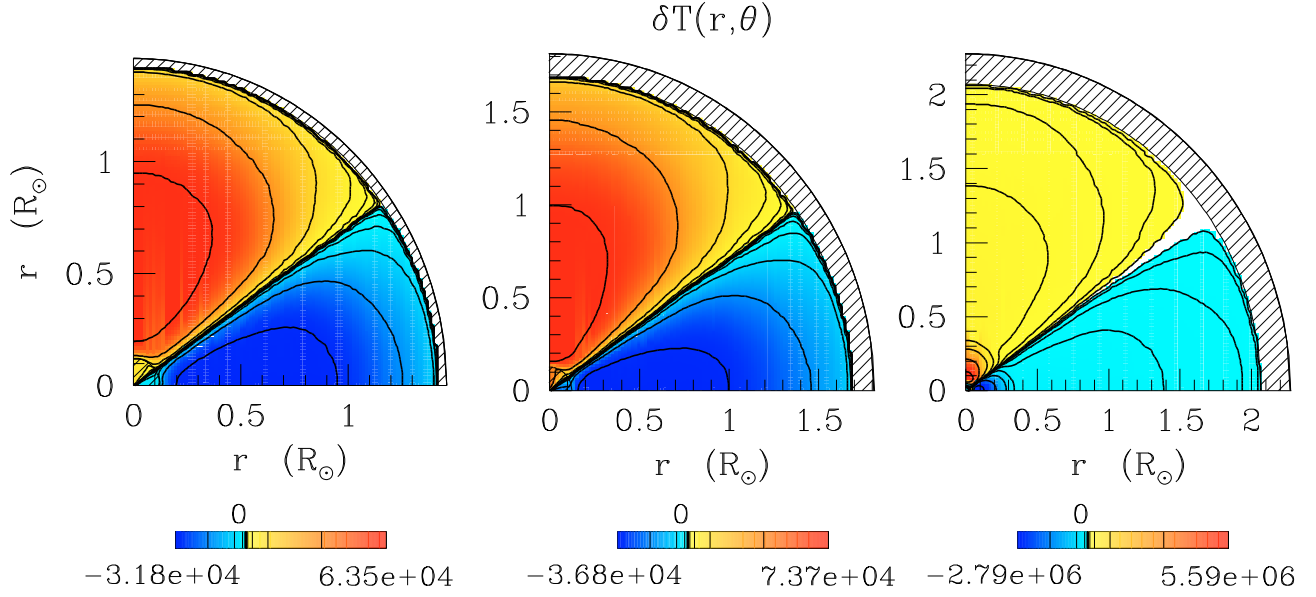


Fig. 13. The temperature fluctuation $\delta T = \bar{T}\Psi_2 P_2(\cos\theta)$ in the $1.5 M_\odot$ model at three different points on the main sequence, when the hydrogen mass fraction in the centre $X_c = 0.675$ (left panel), $X_c = 0.32$ (middle panel), and $X_c = 0$ (right panel).

3.4.3. Possible simplifications

From the previous analysis of the 1.5 and $20 M_\odot$ models, during the quiescent main sequence evolution, the relaxation of Ψ_2 is then ruled approximately by

$$\begin{aligned} & \bar{\rho} \frac{L}{M} \left\{ \frac{2}{3} \left[1 - \frac{\bar{\Omega}^2}{2\pi G \bar{\rho}} \right] \bar{\Omega}^2 \partial_r \left(\frac{r^2}{g} \right) - \frac{2\rho_m}{9} \frac{r^2}{\bar{\rho}} \frac{\partial_r \bar{\Omega}^2}{g} \right. \\ & \left. + \frac{\rho_m}{\bar{\rho}} \left[\frac{r}{3} \partial_r [H_T \partial_r \Psi_2 - (1 - \delta + \chi_T) \Psi_2] - \frac{2H_T}{3r} \left(1 + \frac{D_h}{K_T} \right) \Psi_2 \right] \right\} \\ & \approx \bar{\rho} \bar{T} C_p \frac{N_T^2}{g \delta} U_2. \end{aligned} \quad (42)$$

Note that $\tilde{\mathcal{T}}_{B4}$ is now expressed directly as a function of $\bar{\Omega}$ where Eq. (17) has been used. On the other hand, we have verified that the Λ_2 -terms can be neglected compared to the Ψ_2 ones during the main sequence evolution, which allows simplifications in the writing of $\tilde{\mathcal{T}}_{Th1}$. The advection of entropy is then balanced by $\tilde{\mathcal{T}}_{B1}$, $\tilde{\mathcal{T}}_{B4}$ and the thermal diffusion. The simplification given by Eq. (42) is no longer valid if structural readjustments occur, as is the case when the core contracts at the end of the main sequence. If the Zahn (1992) prescription for D_h is used, the term $\frac{D_h}{K_T}$ can furthermore be omitted.

In conclusion, the picture of the heat transport presented here differs radically from the classical Eddington-Sweet vision where the thermal imbalance induced by the centrifugal acceleration is considered to be at the origin of the meridional circulation. Actually, the circulation is induced by the angular momentum losses and the structural adjustments. Then, it advects entropy, which leads, after thermal relaxation, to a new temperature state and thus to a new differential rotation profile (cf. Eq. (17)). There then remains a circulation induced by the angular momentum losses and the structural adjustments, and the concomitant evolution of the rotation and thermal states.

3.5. Transport of chemicals

Once a composition gradient builds up, due to gravitational settling (not accounted for in the present calculations) or nuclear

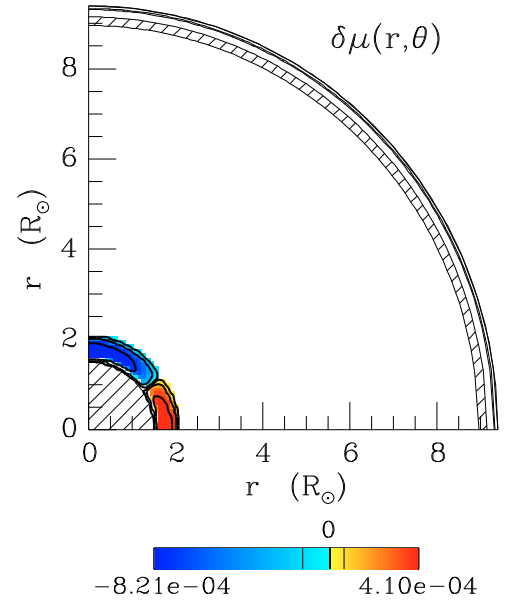


Fig. 14. Two-dimensional reconstruction of the μ -perturbations, $\delta\mu = \bar{\mu}\Lambda_2 P_2(\cos\theta)$, in the $20 M_\odot$ star when $X_c = 0.32$. Hatched regions delineate convection zones.

burning, the meridional circulation creates a latitudinal perturbation of the molecular weight distribution, as described by Eq. (27). The sign of these μ -fluctuations depends on the orientation of the circulation, and we thus expect some differences between the two models.

3.5.1. $20 M_\odot$ model

In that model, the meridional circulation always transports matter with low- μ down to the interior near the rotational axis, while high- μ matter is carried outward along the equator. As a result, a horizontal μ -gradient appears near the convective core (see Fig. 14), which is directed from pole to equator, i.e. opposite to

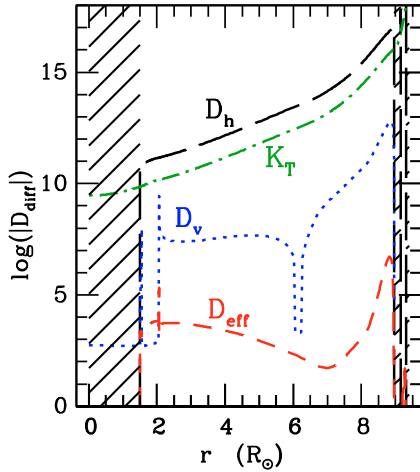


Fig. 15. Profiles of the thermal diffusivity (K_T dotted-dashed green line) and the one that associated to the meridional circulation (D_{eff} short-dashed red line) and with the horizontal (D_h long-dashed black line) and vertical (D_v dotted blue line) turbulence in the $20 M_\odot$ model when $X_c = 0.32$.

that of the temperature fluctuations. These μ -fluctuations remain small (less than 1%), which justifies the perturbative approach.

We already mentioned in Sect. 2.3.4 that the strong turbulent transport in the horizontal direction interferes with the meridional circulation, rendering the vertical transport of diffusive nature, characterised by an effective diffusivity D_{eff} (Chaboyer & Zahn 1992). This description makes the comparison between the two processes that contribute to the transport of chemical elements (vertical shear and combination of advection and horizontal shear) easier since it suffices to compare their respective diffusivities.

This is done in Fig. 15, where we see that in most of the stellar interior the vertical shear turbulence largely dominates the combination of advection and horizontal shear ($D_v \gg D_{\text{eff}}$), except in the vicinity of the convective core, where the strong μ -stratification inhibits the shear instability, and in the region where the gradient of $\bar{\Omega}$ changes sign (and where D_v reduces to the molecular diffusivity).

This figure can be compared with Fig. 6 of Meynet & Maeder (2000), where the same profiles are presented for a $20 M_\odot$ star at $Z = 0.02$, with initial equatorial velocity $v_{\text{ini}} = 300 \text{ km s}^{-1}$. In their simulation, Meynet and Maeder use the prescription given by Eq. (30) for the horizontal turbulent viscosity. While we obtain very similar profiles for the vertical shear diffusion coefficient, D_v , and for the thermal diffusivity, K_T , the diffusion coefficients associated with horizontal turbulence, D_h , and meridional circulation, D_{eff} , differ by several orders of magnitude. The Mathis et al. (2004) prescription results in higher horizontal turbulent viscosity, which also translates into lower D_{eff} . This very same result was first obtained by Maeder (2003), where using energetic considerations, he derived a new expression for D_h that is very similar to Eq. (29) (see also Mathis et al. 2007). It should be noted that the anisotropic turbulence assumption ($D_h \gg D_v$) is always satisfied.

3.5.2. $1.5 M_\odot$ model

Figure 16 shows that the diffusion coefficients in the $1.5 M_\odot$ star are much smaller than in the massive star as a result of lower angular velocity and degree of differential rotation. The diffusion coefficients D_{eff} and D_v are much closer in this model, partly

due to the adoption of Zahn’s (1992) prescription for D_h (see Eqs. (29) and (30) and Mathis et al. 2004, for more details). However, the decreasing efficiency of the meridional transport as the star evolves on the main sequence results in the shear turbulence dominating the distribution of chemicals (see Palacios et al. 2003). The inhibiting action of the composition gradient is visible near the convective core where D_v drops to its microscopic value, indicating that turbulence is suppressed. It should also be noted that the anisotropic turbulence assumption ($D_h \gg D_v$) is also always satisfied in this model.

The sign of the μ -perturbation depends on the orientation of the circulation near the convective core. In the lower mass model, differences arise from the development of a secondary loop, as seen at $X_c = 0.675$ and $X_c = 0$.

Although the meridional circulation and D_h are both smaller in the low-mass star, the ratio U_2/D_h , which governs the relative strength of vertical advection by meridional circulation and of horizontal diffusion (see Eq. (27)), is larger in the $1.5 M_\odot$ compared to the $20 M_\odot$. This results in larger μ -imbalance in the lower-mass model.

4. Conclusion

The paper presents a complete set of diagnostic tools that provide a comprehensive and coherent understanding of the secular hydrodynamical transport processes operating in the radiative zones of rotating stars. The framework is that of “type I rotational mixing”, where angular momentum and nuclides are transported by the same mechanisms, namely large-scale meridional circulation and shear-induced turbulence.

To validate our new approach, the first analysis presented here is performed on two well-studied cases of a low-mass ($1.5 M_\odot$) (see Palacios et al. 2003) and a massive ($20 M_\odot$) star (Meynet & Maeder 2000). It allows us to disentangle the main processes at the origin of meridional circulation and driving angular momentum, heat and chemicals transports in the stellar interior, and to confirm results previously established in the literature. In particular, the angular momentum loss (either by radiation-driven wind as in the massive star or by magnetic braking as in the low-mass star) combined with structural readjustments are the sources responsible for generating meridional circulation (Fig. 18). The direction of the flow is such that it transports angular momentum outward to the surface, except in the deep interior of the $1.5 M_\odot$ star where it can reverse, producing a steeper angular velocity gradient.

This circulation advects heat, and thus generates latitude-dependent temperature fluctuations. These tend to be damped out by radiative diffusion, until they establish a subtle balance between advection and diffusion, which allows them to induce differential rotation through the baroclinic torque (Eq. (17)). This differential rotation is shear-unstable and generates turbulence that participates in the transport of angular momentum, thus closing the loop (Fig. 18). This picture thus differs drastically from the classical Eddington-Sweet circulation, where the circulation is deemed to originate from the thermal imbalance due to the centrifugal force. If turbulent transport and extraction of angular momentum were absent, the circulation would die altogether, as pointed out by Busse (1982).

Thanks to the diagnostic tools we have developed, the present investigation helped to clarify a number of other points. We confirm that it is mainly the meridional circulation that transports angular momentum in the low-mass star (see also Palacios et al. 2003). It is thus crucial to describe that transport as an

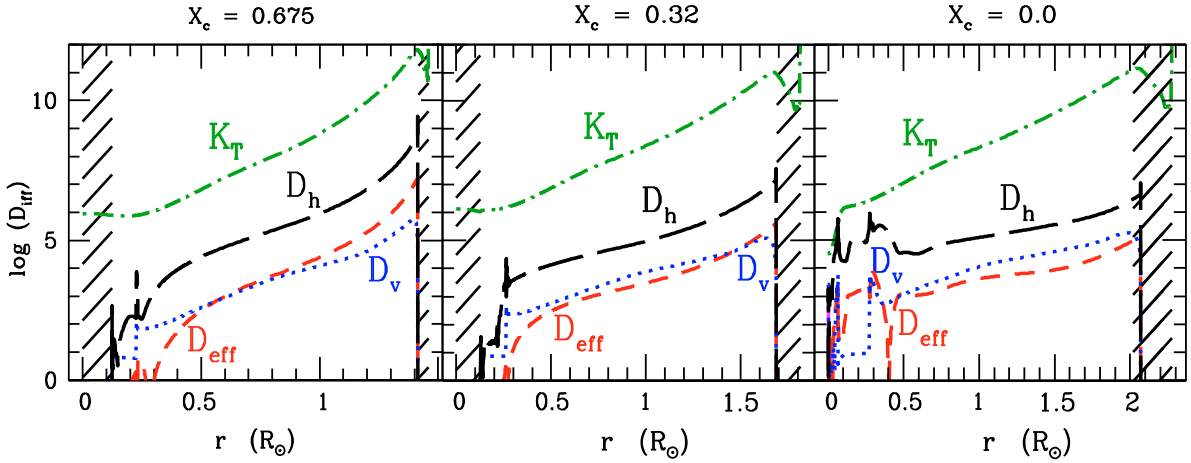


Fig. 16. Same as Fig. 15 for the $1.5 M_{\odot}$ model when $X_c = 0.675$, $X_c = 0.32$, and $X_c = 0.0$.

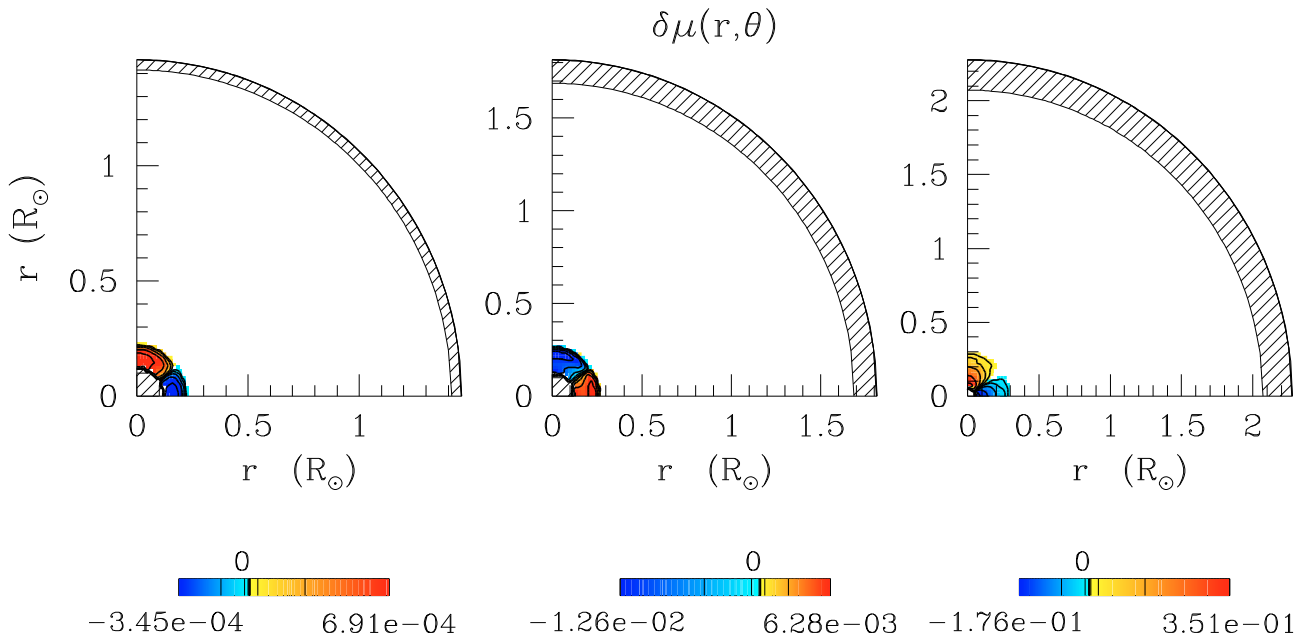


Fig. 17. Two-dimensional reconstruction of the μ -perturbations, $\delta\mu = \bar{\mu}\Lambda_2 P_2(\cos\theta)$ in the $1.5 M_{\odot}$ when $X_c = 0.675$ (left panel), $X_c = 0.32$ (middle panel), and $X_c = 0.0$ (right panel). Hatched regions delineate convection zones.

advective process, as in the approach developed by Zahn, Maeder, and collaborators. In the massive star, where the redistribution of angular momentum due to the star's expansion plays a much more important role than its extraction by the radiative wind, advection and diffusion make comparable contributions, though in different regions. The advective transport dominates in the inner layers of the star, whereas the diffusive transport is the prime actor in the upper part and, moreover, works there in the opposite direction.

For the first time, through detailed computation and separation of the different components, we confirm that the advection of entropy by meridional circulation is almost exactly balanced by the thermal relaxation (barotropic and thermic terms) during most of the main sequence. This was generally assumed prior to the Maeder & Zahn (1998) work integrating the time-dependency of the temperature fluctuations, but not actually verified through the computation. Grounding our detailed analysis in advanced graphical tools, we were also able to propose a simplified expression for the thermal relaxation on the main sequence.

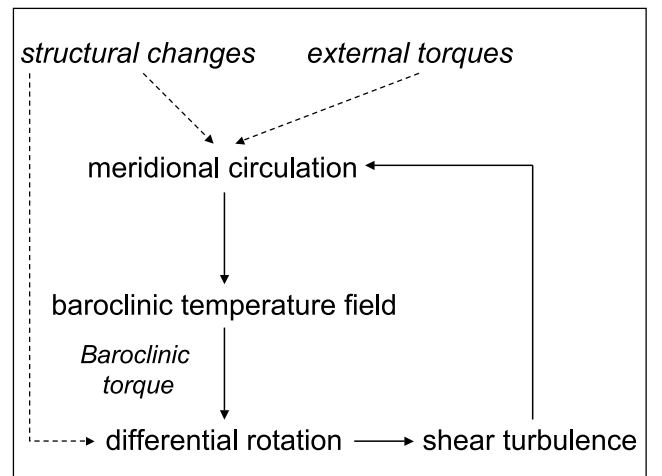


Fig. 18. Rotational mixing of type I in the radiative zone of a rotating star, where the transport of angular momentum is achieved by meridional circulation and turbulent diffusion.

On the other hand, the transport of chemicals is shown to be dominated by the shear-induced turbulence while the star evolves on the main sequence. This is particularly clear for a massive star such as the $20 M_{\odot}$ star.

In the near future, we plan to apply the same tools to type II rotational mixing, where we shall include the transport of angular momentum by internal gravity waves and magnetic stresses and to advanced phases of stellar evolution.

Acknowledgements. We thank the referee A. Maeder for useful remarks that helped in improving the final version of this paper. This work received financial support from the Programme National de Physique Stellaire of CNRS/INSU (France). T.D. and C.C. acknowledge financial support from Swiss FNS. L.S. is FNRS Research Associate. This research has made use of NASA's Astrophysics Data System Bibliographic Services.

Appendix A: Meridional circulation and angular momentum transport

Let us consider the Eq. (11) for the angular momentum transport:

$$\bar{\rho} \frac{d}{dt} (r^2 \bar{\Omega}) = \frac{1}{5r^2} \partial_r (\bar{\rho} r^4 \bar{\Omega} U_2) + \frac{1}{r^2} \partial_r (\bar{\rho} v_v r^4 \partial_r \bar{\Omega}). \quad (\text{A.1})$$

Integrating over a spherical shell, we get

$$\int_{r=r_1}^{r=r_2} \bar{\rho} r'^2 \frac{d}{dt} (r'^2 \bar{\Omega}) dr' = \frac{1}{5} \int_{r=r_1}^{r=r_2} \partial_{r'} (\bar{\rho} r'^4 \bar{\Omega} U_2) dr' + \int_{r=r_1}^{r=r_2} \partial_{r'} (\bar{\rho} v_v r'^4 \partial_r \bar{\Omega}) dr', \quad (\text{A.2})$$

r_1 and r_2 being respectively its inner and outer radius. Then, introducing the elementary mass element $dm = 4\pi \bar{\rho} r^2 dr$, we obtain

$$\frac{1}{4\pi} \int_{m=m(r_1)}^{m=m(r_2)} \frac{d}{dt} (r'^2 \bar{\Omega}) dm = \frac{1}{5} \left[(\bar{\rho} r^4 \bar{\Omega} U_2)_{r=r_2} - (\bar{\rho} r^4 \bar{\Omega} U_2)_{r=r_1} \right] + \left[(\bar{\rho} v_v r^4 \partial_r \bar{\Omega})_{r=r_2} - (\bar{\rho} v_v r^4 \partial_r \bar{\Omega})_{r=r_1} \right]. \quad (\text{A.3})$$

We apply the following identity

$$\frac{d}{dt} \left[\int_{m_1(t)}^{m_2(t)} f(m, t) dm \right] = \int_{m_1(t)}^{m_2(t)} \frac{d}{dt} [f(m, t)] dm + \left\{ \frac{dm_2(t)}{dt} \cdot f(m_2, t) - \frac{dm_1(t)}{dt} \cdot f(m_1, t) \right\}. \quad (\text{A.4})$$

In our Lagrangian description, the mass is conserved, $\frac{dm_2(t)}{dt} = \frac{dm_1(t)}{dt} = 0$, so

$$\frac{1}{4\pi} \frac{d}{dt} \left[\int_{m=m(r_1)}^{m=m(r_2)} r'^2 \bar{\Omega} dm \right] = \frac{1}{5} \left[(\bar{\rho} r^4 \bar{\Omega} U_2)_{r=r_2} - (\bar{\rho} r^4 \bar{\Omega} U_2)_{r=r_1} \right] + \left[(\bar{\rho} v_v r^4 \partial_r \bar{\Omega})_{r=r_2} - (\bar{\rho} v_v r^4 \partial_r \bar{\Omega})_{r=r_1} \right]. \quad (\text{A.5})$$

To obtain the value of the meridional circulation at $m(r)$, we set $r_1 = 0$ and $r_2 = r$:

$$U_2 = \frac{5}{\bar{\rho} r^4 \bar{\Omega}} \left[\Gamma(m) - \bar{\rho} v_v r^4 \partial_r \bar{\Omega} \right] \quad (\text{A.6})$$

where

$$\Gamma(m) = \frac{1}{4\pi} \frac{d}{dt} \left[\int_0^{m(r)} r'^2 \bar{\Omega} dm' \right]. \quad (\text{A.7})$$

Appendix B: Components \mathcal{T}_2 of the heat equation

These terms intervene in the heat relaxation Eq. (18) and their derivation may be found in Zahn (1992) or Mathis & Zahn (2004). They include:

the barotropic term,

$$\mathcal{T}_{2,B} = \frac{2}{3} \left[1 - \frac{\bar{\Omega}^2}{2\pi G \bar{\rho}} - \frac{2}{3} \frac{\rho_m}{\rho} (\varphi \Lambda_2 - \delta \Psi_2) - \frac{(\bar{\epsilon} + \bar{\epsilon}_{\text{grav}})}{\epsilon_m} \right] \bar{\Omega}^2 \partial_r \left(\frac{r^2}{g} \right) - \frac{2}{3} \frac{\rho_m}{\bar{\rho}} (\varphi \Lambda_2 - \delta \Psi_2); \quad (\text{B.1})$$

the thermic term,

$$\mathcal{T}_{2,Th} = \frac{\rho_m}{\bar{\rho}} \left[\frac{r}{3} \partial_r \mathcal{A}_2(r) - \frac{2H_T}{3r} \left(1 + \frac{D_h}{K_T} \right) \Psi_2 \right]; \quad (\text{B.2})$$

the term associated with local energy sources,

$$\mathcal{T}_{2,N-G} = \frac{(\bar{\epsilon} + \bar{\epsilon}_{\text{grav}})}{\epsilon_m} [\mathcal{A}_2(r) + (f_{\epsilon} \epsilon_T - f_{\epsilon} \delta + \delta) \Psi_2 + (f_{\epsilon} \epsilon_{\mu} + f_{\epsilon} \varphi - \varphi) \Lambda_2],$$

where

$$\mathcal{A}_2(r) = H_T \partial_r \Psi_2 - (1 - \delta + \chi_T) \Psi_2 - (\varphi + \chi_{\mu}) \Lambda_2. \quad (\text{B.3})$$

Here, $N_T^2 = (\bar{g} \delta / H_P) (\nabla_{\text{ad}} - \nabla)$ is the square of the thermal part of the Brünt-Väisälä frequency where $\nabla = \partial \ln T / \partial \ln P$ is the radiative temperature gradient and ∇_{ad} is the adiabatic one. The variables L , M , C_P have their usual meaning and \bar{T} is the horizontal average of the temperature. We also introduced the pressure and temperature scale-heights $H_P = |dr/d \ln P|$ and $H_T = |dr/d \ln \bar{T}|$, the thermal diffusivity $K_T = \bar{\chi} / \bar{\rho} C_P = 16 \sigma T^3 / 3 \kappa \bar{\rho}^2 C_P$, the horizontal eddy-diffusivity D_h and $f_{\epsilon} = \bar{\epsilon} / (\bar{\epsilon} + \bar{\epsilon}_{\text{grav}})$, with $\bar{\epsilon}$ and $\bar{\epsilon}_{\text{grav}}$ being the mean nuclear and gravitational energy release rates, respectively. Both σ and κ are the Stefan constant and the Rosseland mean opacity, and $\epsilon_{\mu} = (\partial \ln \epsilon / \partial \ln \mu)_{P,T}$ and $\chi_{\mu} = (\partial \ln \chi / \partial \ln \mu)_{P,T}$ are the logarithmic derivatives of ϵ and of the radiative conductivity χ with respect to μ , and $\epsilon_T = (\partial \ln \epsilon / \partial \ln T)_{P,\mu}$ and $\chi_T = (\partial \ln \chi / \partial \ln T)_{P,\mu}$ are the derivatives of these same quantities with respect to the temperature T . Finally $\epsilon_m = L/M$ and $\rho_m = 3\bar{g}(r)/4\pi r G$ are the horizontal average of the energy production rate and the mean density inside the considered level surface.

References

- Abt, H. A., Levato, H., & Grosso, M. 2002, *ApJ*, 573, 359
 Bouret, J. -C., Donati, J. -F., Martins, F., et al. 2008, *MNRAS*, 389, 75
 Braithwaite, J. 2006, *A&A*, 449, 451
 Braithwaite, J., & Spruit, H. 2005, *Nature*, 431, 819
 Brun, A.-S., & Zahn, J.-P. 2006, *A&A*, 457, 665
 Busse, F. H. 1982, *ApJ*, 259, 759
 Chaboyer, B., & Zahn, J.-P. 1992, *A&A*, 253, 173
 Charbonnel, C., & Talon, S. 2005, *Science*, 309, 2189
 Charbonneau, P., & MacGregor, K. B. 1993, *ApJ*, 417, 762
 Decressin, T., Meynet, G., Charbonnel, C., Prantzos, N., & Ekström, S. 2007, *A&A*, 464, 1029
 Eddington, A. S. 1925, *Obs*, 48, 73
 Ekström, S., Meynet, G., Maeder, A., & Barblan, F. 2008, *A&A*, 478, 467
 Eggenberger, P., Maeder, A., & Meynet, G. 2005, *A&A*, 440, L9
 Endal, A. S., & Sofia, S. 1978, *ApJ*, 220, 279
 Espinosa Lara, F., & Rieutord, M. 2007, *A&A*, 470, 1013
 Fukada, I. 1982, *PASP*, 94, 271

- Gaigé, Y. 1993, *A&A*, 269, 267
 Garaud, P. 2002a, *MNRAS*, 329, 1
 Garaud, P. 2002b, *MNRAS*, 335, 707
 Grevesse, N., Noels, A., & Sauval, A. J. 1996, *Cosmic Abundances*, 99, 117
 Heger, A., Langer, N., & Woosley, S. E. 2000, *ApJ*, 528, 368
 Henyey, L. G., Forbes, J. E., & Gould, N. L. 1964, *ApJ*, 139, 306
 Kawaler, S. D. 1988, *ApJ*, 333, 236
 Kippenhahn, R., & Weigert, A. 1990, *Stellar Structure and Evolution* (Springer-Verlag)
 Maeder, A. 1999, *A&A*, 347, 185
 Maeder, A. 2002, *A&A*, 392, 575
 Maeder, A. 2003, *A&A*, 399, 263
 Maeder, A. 2009, *Physics, Formation and Evolution of Rotating Stars* (Springer-Verlag)
 Maeder, A., & Zahn, J.-P. 1998, *A&A*, 334, 1000
 Maeder, A., & Meynet, G. 2000a, *A&A*, 361, 159
 Maeder, A., & Meynet, G. 2000b, *ARA&A*, 38, 143
 Maeder, A., & Meynet, G. 2001, *A&A*, 373, 555
 Maeder, A., & Meynet, G. 2004, *A&A*, 422, 225
 Mathis, S., & Zahn, J.-P. 2004, *A&A*, 425, 229
 Mathis, S., & Zahn, J.-P. 2005, *A&A*, 440, 653
 Mathis, S., Palacios, A., & Zahn, J.-P. 2004, *A&A*, 425, 243
 Mathis, S., Palacios, A., & Zahn, J.-P. 2007, *A&A*, 462, 1063
 Mathis, S., Talon, S., Pantillon, F.-P., & Zahn, J.-P. 2008, *Sol. Phys.*, 251, 101
 Menou, K., Balbus, S. A., & Spruit, H. C. 2004, *ApJ*, 607, 564
 Mestel, L. 1953, *MNRAS*, 113, 716
 Meynet, G., & Maeder, A. 2000, *A&A*, 361, 101
 Meynet, G., Ekström, S., Maeder, A., & Barblan, F. 2007, *ASP*, 361, 325
 Palacios, A., Talon, S., Charbonnel, C., & Forestini, M. 2003, *A&A*, 399, 603
 Palacios, A., Charbonnel, C., Talon, S., & Siess, L. 2006, *A&A*, 453, 261
 Pantillon, F. P., Talon, S., & Charbonnel, C. 2007, *A&A*, 474, 155
 Pinsonneault, M. H., Kawaler, S. D., Sofia, S., & Demarque, P. 1989, *ApJ*, 338, 424
 Press, W.-H. 1981, *ApJ*, 245, 286
 Reimers, D. 1975, *Mémoires de la Société Royale des Sciences de Liège*, 8, 369
 Rieutord, M. 2006a, *Stellar Fluid Dynamics and Numerical Simulations: from the Sun to Neutron Stars*, ed. M. Rieutord, & B. Dubrulle, *EAS*, 21, 275
 Rieutord, M. 2006b, *A&A*, 451, 1025
 Rogers, T., & Glatzmaier, G. 2005, *MNRAS*, 364, 1135
 Schatzman, E. 1962, *Ann. Astrophys.*, 25, 18
 Schatzman, E. 1993, *A&A*, 279, 431
 Schnerr, R. S., Henrichs, H. F., Neiner, C., et al. 2008, *A&A*, 483, 857
 Spruit, H. C. 1999, *A&A*, 349, 189
 Spruit, H. C. 2002, *A&A*, 381, 923
 Siess, L. 2006, *A&A*, 448, 717
 Siess, L., Dufour, E., & Forestini, M. 2000, *A&A*, 358, 593
 Sweet, P. A. 1950, *MNRAS*, 110, 548
 Talon, S. 1997, Ph.D. Thesis, Université Paris 7
 Talon, S. 2008, in *EAS Publications Series*, ed. C. Charbonnel, & J.-P. Zahn, *EAS Publ. Ser.*, 32, 81
 Talon, S., & Zahn, J.-P. 1997, *A&A*, 317, 749
 Talon, S., & Charbonnel, C. 1998, *A&A*, 335, 959
 Talon, S., & Charbonnel, C. 2003, *A&A*, 405, 1025
 Talon, S., & Charbonnel, C. 2004, *A&A*, 418, 1051
 Talon, S., & Charbonnel, C. 2005, *A&A*, 440, 981
 Talon, S., & Charbonnel, C. 2008, *Proc. IAU Symp.*, 252 [arXiv:0805.4697]
 Talon, S., Kumar, P., & Zahn, J.-P. 2002, *ApJ*, 574, L175
 Talon, S., Zahn, J.-P., Maeder, A., & Meynet, G. 1997, *A&A*, 322, 209
 Vink, J. S., de Koter, A., & Lamers, H. J. G. L. M. 2000, *A&A*, 362, 295
 Vogt, H. 1925, *AN*, 223, 229
 Zahn, J.-P. 1992, *A&A*, 265, 115
 Zahn, J.-P., Brun, A. S., & Mathis, S. 2007, *A&A*, 474, 145